

1 Optimal Stacking of Noise Cross-Correlation Functions

2 Xiaotao Yang^{1,2*}, Jared Bryan³, Kurama Okubo^{1,4}, Chengxin Jiang^{1,5},

3 Timothy Clements^{1,6}, and Marine A. Denolle^{1,7}

¹ Department of Earth and Planetary Sciences, Harvard University. Cambridge, MA, USA

² Now at Department of Earth, Atmospheric, and Planetary Sciences, Purdue University. West Lafayette, IN, USA

³ Department of Earth, Atmospheric, and Planetary Sciences, Massachusetts Institute of Technology. Cambridge, MA USA

⁴ Now at National Research Institute for Earth Science and Disaster Resilience, Tsukuba, Japan

⁵ Now at Research School of Earth Sciences, Australian National University. Acton, ACT Australia

⁶ Now at Earthquake Science Center, United States Geological Survey. Moffet Field, CA USA

⁷ Now at Department of Earth and Space Sciences, University of Washington, Seattle, WA USA

4 Received –; in original form –

5 SUMMARY

6 Cross-correlations of ambient seismic noise are widely used for seismic velocity imaging, mon-
7 itoring, and ground motion analyses. A common step in analyzing Noise Cross-correlation
8 Functions (NCFs) is stacking short-term NCFs over longer time periods to increase the sig-
9 nal quality. Spurious NCFs could contaminate the stack, degrade its quality, and limit its use.
10 Many methods have been developed to improve the stacking of coherent waveforms, includ-
11 ing earthquake waveforms, receiver functions, and NCFs. This study systematically evaluates
12 and compares the performance of eight stacking methods: arithmetic mean or linear stacking,
13 robust stacking, selective stacking, cluster stacking, phase-weighted stacking, time-frequency
14 phase-weighted stacking, N^{th} -root stacking, and averaging after applying an adaptive covari-
15 ance filter. Our results demonstrate that, in most cases, all methods can retrieve clear ballistic or
16 first arrivals. However, they yield significant differences in preserving the phase and amplitude
17 information. This study provides a practical guide for choosing the optimal stacking method for
18 specific research applications in ambient noise seismology. We evaluate the performance using
19 multiple onshore and offshore seismic arrays in the Pacific Northwest region. We compare these
20 stacking methods for NCFs calculated from raw ambient noise (referred to as Raw NCFs) and
21 from ambient noise normalized using a one-bit clipping time normalization method (referred to
22 as One-bit NCFs). We evaluate six metrics, including signal-to-noise ratios, phase dispersion
23 at individual station pairs, convergence rate, temporal changes in the ballistic and coda waves,
24 relative amplitude decays with distance, and computational time. For seismic velocity tomog-

25 raphy, we show that robust stacking is the best for imaging using Raw NCFs, that all methods
26 but phase-weighted and N^{th} -root stacking perform equally well for One-bit NCFs. For moni-
27 toring applications, robust stacking is the best when using Raw NCFs while linear, robust, and
28 selective stacking methods are all equally appropriate choices when using One-bit NCFs. For
29 applications relying on accurate relative amplitudes, robust stacking should be used for Raw
30 NCFs while both the robust and cluster stacking methods both perform well for One-bit NCFs.
31 The evaluations in this study can be generalized to a broad range of time-series analysis that
32 utilizes data coherence to perform ensemble stacking. Another contribution of this study is the
33 accompanied open-source software, which can be used for general purposes.

34 **Key words:** Seismic interferometry, Seismic tomography, Earthquake ground motions, Seis-
35 mic noise, Time-series analysis, Coda waves

36 1 INTRODUCTION

37 Cross-correlations of ambient seismic noise have been widely used to image the Earth's elastic (L. Feng and Ritzwoller 2019;
 38 Shapiro et al. 2005; S.-M. Wu et al. 2021; X. Yang and Gao 2018, 2020) and anelastic structure (Prieto et al. 2009), model
 39 ground motions (Denolle et al. 2013, 2014, 2018; Kwak et al. 2017; Viens and Denolle 2019; Viens et al. 2017), and monitor
 40 transient velocity changes in the shallow subsurface (F. Brenguier et al. 2008; Clements and Denolle 2018; Donaldson et
 41 al. 2019; K.-F. Feng et al. 2021; Olivier et al. 2019; Wang et al. 2017; Z. Yang et al. 2022). The Noise Cross-correlation
 42 Functions (NCFs) are typically computed in short-time windows (such as hours or days) after diverse pre-processing on the
 43 raw ambient noise waveforms (Bensen et al. 2007; L. Feng and Ritzwoller 2019). Stacking of NCFs over a longer period
 44 (such as weeks, months, or years) is a common procedure for most applications utilizing NCFs (e.g., Seats et al. 2012). For
 45 seismic tomography, the final stack over the entire time period is used to make waveform or travel-time measurements. Seismic
 46 monitoring requires stacking over a subset of time windows, balancing between the temporal resolution and the coherence
 47 of the NCFs (Hadziioannou et al. 2011). Both applications rely on the phase information of ballistic (first arrival) and coda
 48 waves. Studies of ground motion prediction and attenuation tomography, on the other hand, require accurate relative amplitude
 49 measurements between station pairs. Because NCFs consist primarily of dispersive surface waves, preserving the relative
 50 amplitude would also preserve the spectral content. Therefore, the performance of stacking and the preservation of either
 51 phase or amplitude information are important to ensure the robustness of the scientific results.

52 The most commonly used stacking method is the arithmetic mean of the data over temporal or spatial samples, referred to
 53 as Linear stacking. For NCFs, substantial temporal variation may exist across individual short time windows, which could result
 54 from the seasonal change of the location and strength of the microseismic sources (Bensen et al. 2007; L. Ermert et al. 2016;
 55 L. A. Ermert et al. 2021; Tian and Ritzwoller 2017; X. Yang et al. 2019), disruption from tectonic signals (Baig et al. 2009),
 56 or unknown instrumental failures. It is important to use an appropriate stacking method to extract coherent NCFs, particularly
 57 when strong variations of the data quality present. Besides Linear stacking, many more advanced methods have been developed
 58 to improve the stacking of NCFs, and time-series data in general. Rückemann (2012) provides a summary of the theoretical
 59 background of several stacking methods to improve the common-mid-point gathers in seismic reflection data. A systematical
 60 evaluation of the performance of different stacking methods in processing real NCF data is highly desirable.

61 In this paper, we compare the eight algorithms used for stacking NCFs and evaluate their performance for canonical
 62 research applications. These methods include: robust stacking (Pavlis and Vernon 2010), selective stacking (modified from
 63 Olivier et al. 2015), cluster stacking (a new method), Phase-Weighted Stacking PWS Schimmel and Paulssen 1997), time-
 64 frequency Phase-Weighted Stacking (tf-PWS) (Baig et al. 2009; Li et al. 2017; Schimmel and Gallart 2007; Schimmel et al.
 65 2011; Thurber et al. 2014; Zeng and Thurber 2016), N^{th} -root stacking (Millet et al. 2019; Rückemann 2012), and linear
 66 stacking after applying an Adaptive Covariance Filter (Nakata et al. 2015). We exclude the stacking methods that use the
 67 curvelet transform (Baig et al. 2009) and singular value decomposition (Moreau et al. 2017), as these focus specifically on

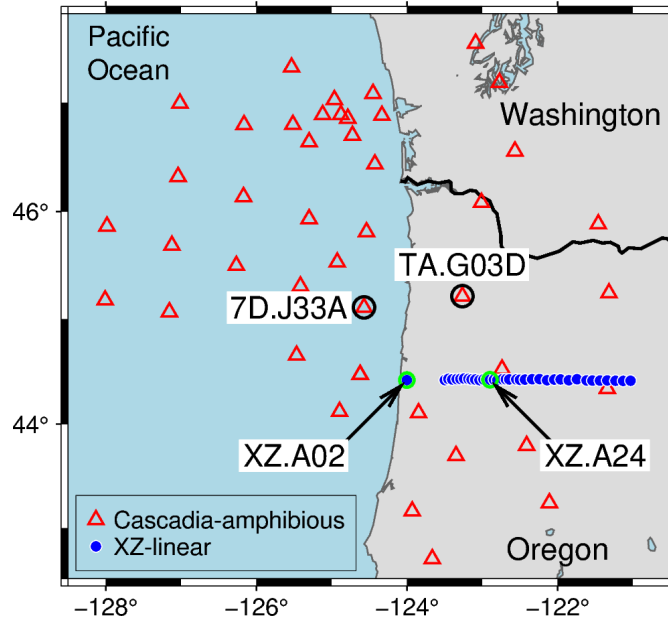


Figure 1. Seismic stations used in this study. The USArray Transportable Array and Cascadia Initiative Ocean Bottom Seismographs (red open triangles) form a composite dataset that is referred to as the "Amphibious" dataset. The 1993-1994 Cascadia broadband XZ linear array (blue dots) is referred to as the "XZ" dataset. Labeled stations are used as virtual sources and receivers in the examples in this paper.

68 short-term convergence alone. We assess the performance of the eight algorithms using six different metrics relevant to specific
 69 research applications. Because the one-bit pre-processing is designed to reduce the influence of earthquake-like transient signals
 70 and to improve the quality of individual NCFs (Bensen et al. 2007), we benchmark our tests using both the raw and one-bit
 71 normalization pre-processing techniques. The development of new methods, computer codes, and performance tests from this
 72 study aim to guide the community in choosing the appropriate stacking method for ambient-noise seismology use cases, though
 73 they can also be generalized to process other time-series data.

74 2 AMBIENT NOISE CROSS-CORRELATIONS

75 This study uses the Pacific Northwest as a natural laboratory (Fig. 1). We gather data from 29 Cascadia Initiative Ocean
 76 Bottom Seismographs (OBS) (network code: 7D; https://doi.org/10.7914/SN/7D_2011), 15 US Transportable Array
 77 stations (network code: TA; <https://doi.org/10.7914/SN/TA>), and 43 stations from the 1993-1994 Cascadia subduction
 78 zone experiment (network code: XZ; Nabelek et al. 1993). We group the data into two datasets: 1) the composite dataset from
 79 the Cascadia Initiative OBSs and onshore TA stations is referred to as the "Amphibious" dataset; 2) the data from the East-West
 80 XZ linear array in northern Oregon is referred to as the "XZ" dataset. All data are publicly accessible from the seismic data
 81 archive of the Incorporated Research Institutions for Seismology Data Management Center (IRIS DMC).

82 We use the *SeisGo* Python toolbox to download the continuous seismic waveforms and compute the NCFs (X. Yang et al.
 83 2022a). The cross-correlation function in *SeisGo* was modified from *NoisePy* (Jiang and Denolle 2020). We download the
 84 vertical component of the continuous waveforms in 12-hour segments. We select data from 10/1/2011 to 7/31/2012 for the

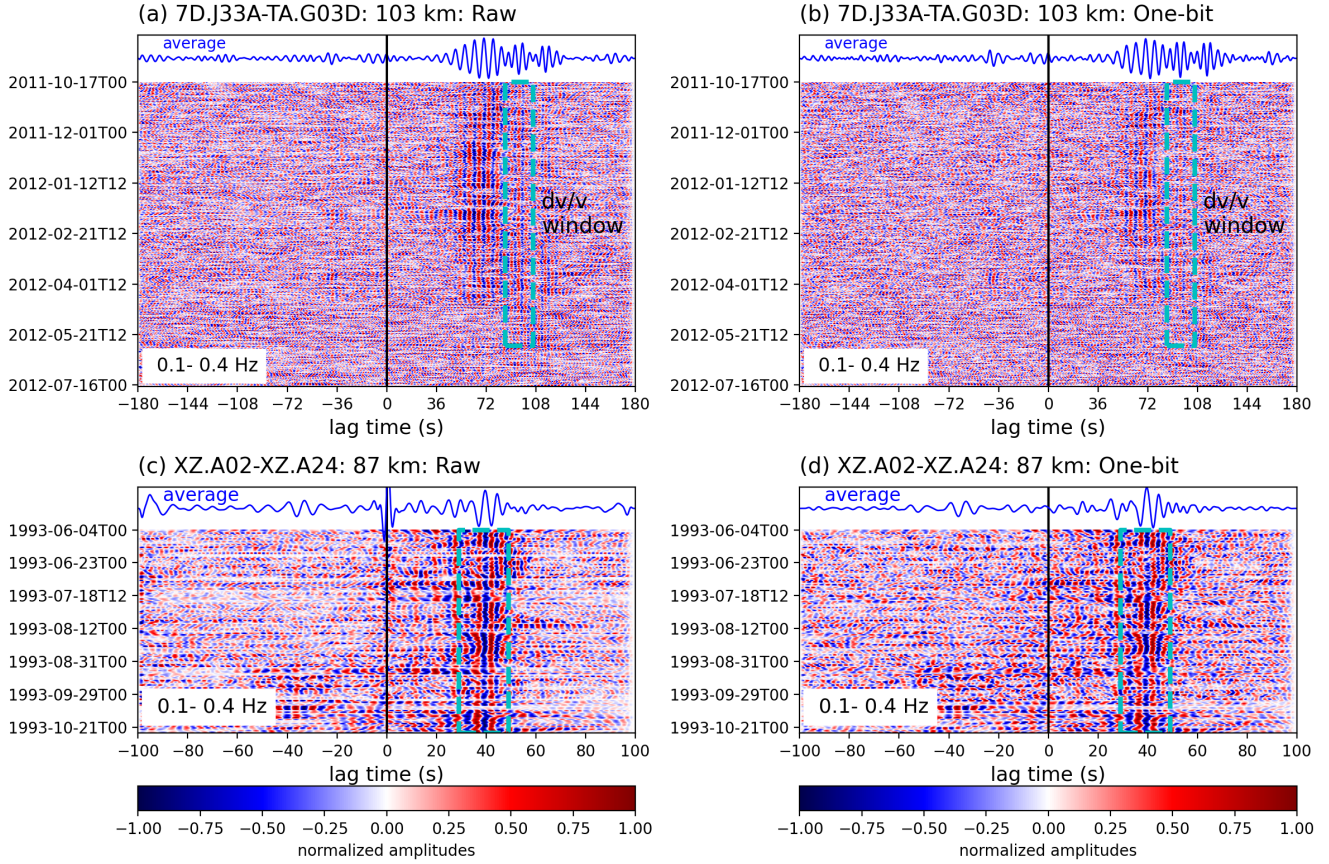


Figure 2. Examples of ambient noise cross-correlation functions (NCFs) between (a-b) OBS station 7D.J33A and onshore station TA.G03D and (c-d) XZ linear array stations XZ.A02 and XZ.A24. The NCFs are filtered at 0.1-0.4 Hz. The left panels are NCFs computed with raw waveforms and the right panels are NCFs computed after applying one-bit time-domain normalization. The dashed cyan boxes mark the windows used for the analysis of the preservation of transient phase changes (Section 4.4) using (a-b) coda waves and (c-d) ballistic phases. On the top of each panel, we show the linear stack as arithmetic averages. The NCFs are color-coded by the normalized amplitudes (red is 1, blue is -1).

85 Amphibious dataset and from 6/1/1993 to 5/31/1994 for the XZ dataset. We remove the instrument responses and convert
 86 the data to displacements, followed by down-sampling to 5 samples per second. We compute the NCFs in 6-hour windows
 87 sliding every 3 hours. The data is demeaned and detrended for each 6-hour segment. We attempt to remove transient signals
 88 in the ambient noise that will contaminate the noise cross correlations by removing the windows with anomalous amplitudes.
 89 For that, we calculate the maximum absolute raw noise amplitude of the segment and the standard deviation of the raw noise
 90 amplitudes of all segments. We discard waveform segments with peak amplitudes greater than 10 times the standard deviation,
 91 as implemented in *NoisePy*.

92 We construct two sets of cross-correlations using the raw waveforms (Viens et al. 2017) and waveforms normalized in the
 93 time domain using the `sign` function (e.g., Bensen et al. 2007; Shen et al. 2012). We denote the two datasets as Raw NCFs and
 94 One-bit NCFs, respectively. To avoid spectral leakage, the short 6-hour time windows are tapered using a Tukey window with
 95 a cosine fraction of 0.05. We then apply a Fourier transform to the short-window segment and compute the cross-correlation in

96 the frequency domain using the following equation:

$$X = \mathcal{F}^{-1}(\mathcal{F}^*(d_s)\mathcal{F}(d_r)), \quad (1)$$

97 where X is the NCF between time series d_s (virtual source) and d_r (receiver), \mathcal{F} is the Fourier transform operator, \mathcal{F}^* stands
98 for the complex conjugate of the Fourier transform, and \mathcal{F}^{-1} is the inverse Fourier transform operator.

99 We show a few examples of the computed NCFs (bandpass filtered at 0.1-0.4 Hz) in Fig. 2 for both pre-processing strate-
100 gies. The asymmetry of the NCF is a known effect of noise source directionality (Stehly et al. 2006). The first-order observation
101 is that the individual NCFs contain incoherent noise that may overwhelm the coherent signals. The NCFs from the XZ land
102 station pair all show clear ballistic phases (Fig. 2c-d). For the amphibious station pair 7D.J33A-TA.G03D, clear ballistic phases
103 are present between 50s and 100s for most of the NCFs between October 2011 and April 2012, for both Raw NCFs (Fig. 2a) and
104 One-bit NCFs (Fig. 2b). However, the ballistic phases are almost invisible for the NCFs after May 2012. These "noisy" NCFs
105 may contaminate the linear stack of the NCFs. The simple time-domain representation in Fig. 2 only provides a qualitative
106 visual assessment. We later quantify the performance using different stacking methods with multiple metrics.

107 3 STACKING METHODS

108 This section describes the algorithms beyond the arithmetic mean (or Linear stacking) for optimally stacking NCFs. Most of
109 these methods are adapted from the literature.

110 3.1 Robust stacking

111 Pavlis and Vernon (2010) first introduced Robust stacking to improve the accuracy of picking phase arrival times in seismo-
112 grams from teleseismic earthquakes. We adapt this generic, iterative, weighted stacking method to process NCFs. The weights
113 in Robust stacking penalize the NCFs that deviate too much from a reference stack based on waveform de-coherence. The
114 weight w_i of the i^{th} NCF, \mathbf{d}_i , is calculated as:

$$w_i^j = \frac{|\mathbf{b}_j \cdot \mathbf{d}_i|}{\|\mathbf{d}_i\| \|\mathbf{r}_i\|}, \quad (2)$$

115 where \mathbf{b}_j is the reference stack of the j^{th} iteration, and $\mathbf{r}_i = \mathbf{b}_j - (\mathbf{b}_j \cdot \mathbf{d}_i)\mathbf{d}_i$ is the residual between the current reference stack
116 and the i^{th} NCF scaled by the dot product of the two time series. The weights can be calculated over either the entire NCF or
117 a specific time window that contains the seismic phase of interest. For examples in this paper, we compute the weights over
118 the entire NCF, though our software package allows the user to specify the time window. After computing the weights for all
119 NCFs, we normalize them to their sum and use them to produce the updated stack.

120 The initial reference stack \mathbf{b}_1 is chosen as the median NCF, following the observation of Pavlis and Vernon (2010) that the
121 median is more representative of the concentration of data in the presence of outliers. In our implementation, the users may

122 specify another trace as the initial stack, such as the Linear stack for example. The iterative procedure stops when a convergence
 123 criterion is satisfied. We adopt the criterion proposed by Pavlis and Vernon (2010):

$$\frac{|\mathbf{b}_j - \mathbf{b}_{j-1}|}{\|\mathbf{d}_i\|M} < \epsilon, \quad (3)$$

124 where M is the number of samples in each NCF time-series and ϵ is a small number, with a default value of 10^{-5} .

125 3.2 Selective stacking

126 In the presence of strong noise, it could be effective to stack only a subset of the NCF ensemble that exceeds a quality threshold
 127 and to ignore the low-quality NCFs. This concept, called selective stacking, has been implemented in previous studies (e.g.,
 128 Olivier et al. 2015; Thangraj and Pulliam 2021). The signal-to-noise ratio (SNR) or the correlation to the reference can be
 129 used to evaluate the quality of each NCF. Olivier et al. (2015) used the SNR around the expected S-wave arrival time to
 130 reconstruct S-waves in the stacked NCF. Liu et al. (2009) proposed the weighted stack of common-midpoint gather using the
 131 local correlation within the moving window to improve the SNR and to suppress the random noise in the stacked trace. To
 132 enhance the coherence of the signal, we use a criterion based on the similarity between each NCF and the reference NCF. In
 133 our implementation, by default, the reference NCF is initialized as the Linear stack of the entire ensemble (similar to Liu et al.
 134 2009). As in Robust stacking, the user can specify any trace (e.g., the median NCF) as the reference stack and the window used
 135 to estimate the similarity.

136 Selective stacking sets the weights of low-similarity NCFs to zero when Robust stacking would probably have relatively
 137 low weights. Here, the similarity is quantified as the Pearson correlation coefficient between the reference stack and each
 138 NCF. Note that the criteria used in this study is equivalent to the global correlation described in Liu et al. (2009) rather than
 139 the local correlation for the sake of simplicity in the thresholding. A similarity threshold allows us to discriminate the set of
 140 NCFs to keep or discard (weight is set to zero). We then compute the Linear stack over the subset of NCFs with a Pearson
 141 correlation coefficient above the threshold and discard the NCFs below the threshold. Similar to robust stacking, we implement
 142 the selective stacking method in an iterative scheme, with the same convergence criterion as in Equation 3. In our examples,
 143 we use a threshold correlation coefficient of 0.

144 3.3 Cluster stacking

145 An alternative method to ranking waveforms according to a specific similarity metric is to group them into clusters and perform
 146 the stack for each cluster. Viens and Iwata (2020) proposed the idea of clustering the NCFs using a dimensionality reduction
 147 technique (principal component analysis). In our implementation, we use the *Tslearn* Python toolkit (Tavenard et al. 2020) for
 148 k-means clustering of the NCFs waveforms based on the euclidean distance. We impose two clusters to separate NCFs with
 149 higher quality from those with lower quality.

150 After clustering the NCFs into two clusters, the final stack \mathbf{b} is computed as a weighted stack of the two cluster centers

$$\mathbf{b} = \sum_{i=1,2} w_i C_i, \quad (4)$$

151 where C_i ($i=1, 2$) are the centers (sample averages or linear stacks) of the two clusters and w_i ($i=1, 2$) are the weights of the
152 cluster centers. The center stacking weights, w_i ($i=1, 2$), are computed as

$$w_{i=1,2} = \begin{cases} \begin{cases} 0, & p_i < \max(p_1, p_2) \\ 1, & p_i \geq \max(p_1, p_2) \end{cases}, & cc < h \\ p_i / (p_1 + p_2), & cc \geq h \end{cases}, \quad (5)$$

153 where cc is the correlation coefficient between the two cluster centers C_1 and C_2 , h is the similarity threshold specified by the
154 user, and p_i ($i=1, 2$) are the relative peak amplitude of the cluster center, computed as the ratio of the maximum and root-mean-
155 square of the absolute amplitudes. In our examples, p_1 and p_2 are computed over the entire NCF. Our implementation also
156 allows the user to specify the window of interest to compute the maximum of the absolute amplitudes. According to Equation
157 5, the two centers are weighted by the relative peak amplitude when their correlation coefficient exceeds the threshold ($h=0.75$
158 for our examples). Otherwise, we use the center with a higher peak amplitude as the final stack.

159 3.4 Phase-weighted stacking

160 Phase-weighted stacking (PWS) computes the weight for each trace by the coherency of the instantaneous phases (Schimmel
161 and Paulssen 1997). Our implementation of the PWS method follows the description in Schimmel and Paulssen (1997). The
162 readers are referred to Schimmel and Paulssen (1997) for detailed equations and procedures of the PWS method. The final stack
163 is constructed as a non-linear weighted stack where each sample is weighted by the instantaneous phase. The key parameter
164 for PWS is a harshness parameter that quantifies the fall-off of the weight of each NCF with decreasing similarity. We set the
165 harshness to 2, as in Schimmel and Paulssen (1997).

166 3.5 Time-frequency phase-weighted stacking

167 Schimmel and Gallart (2007) and Schimmel et al. (2011) proposed an improved phase-weighted stacking method that computes
168 the weight in both the time and frequency domains. This method, referred to as tf-PWS, projects each seismic trace into the
169 time-frequency domain through the Stockwell transform (S-transform; Stockwell et al. 1996). Baig et al. (2009) adapted the
170 stacking method based on a more efficient discrete orthogonal S-transform that is introduced by Stockwell (2007). The imple-
171 mentation of tf-PWS in this study follows the description by Schimmel et al. (2011) using the original S-transform (Equations
172 4-7 therein). Similar to PWS, the tf-PWS is primarily controlled by a harshness parameter that determines the sharpness of the
173 transition between phase similarity and dissimilarity. We set the harshness to 2 for our examples, as in Schimmel et al. (2011).

174 3.6 N^{th} -root stacking

175 N^{th} -root stacking method is commonly employed in array seismology (Birtbill et al. 1968; Kanasewich et al. 1973; Millet
176 et al. 2019; Rost and Thomas 2002; Rückemann 2012; Schimmel and Paulssen 1997). It is a nonlinear stacking method that
177 takes the N^{th} -root of the absolute amplitudes of each individual trace and sums them together. The summation is then raised to
178 the power of N to assign the sample weight. The polarity of each sample is recovered with a sign function of the summation.
179 Our implementation follows the description in Millet et al. (2019) (their equation 18). We use the square root (i.e., $N=2$) in our
180 study.

181 3.7 Adaptive covariance filter stacking

182 Nakata et al. (2015) introduced an adaptive covariance filter (ACF) to suppress incoherent noise in seismic data based on
183 the adaptive polarization filter (Du et al. 2000; Samson and Olson 1981). We implement the ACF stacking method following
184 Nakata et al. (2015). The final stack is the Linear stack after applying the ACF. We use 1 as the harshness of the filter.

185 4 EVALUATION AND COMPARISON OF STACKING ALGORITHMS

186 We implement the stacking algorithms described in Section 3 as a standalone Python package *StackMaster* (X. Yang
187 et al. 2022b). The package is available as a repository on Python Package Index (PyPI). It can be installed with:
188 `pip install stackmaster`. In this paper, we install *StackMaster* with the *SeisGo* toolbox (X. Yang et al. 2022a) under
189 the same Anaconda environment. We apply the stacking techniques to the Amphibious and the XZ datasets. Fig. 3 shows the
190 stacking results for the two station pairs in Fig. 2. Figs 4-9 are the stacking results of all station pairs from the virtual sources
191 at 7D.J33A (Figs 4-6) and at XZ.A02 (Figs 8-9).

192 We then evaluate and compare the performance of these stacking methods. Recognizing that NCFs are used in multiple
193 applications (e.g., seismic velocity tomography, monitoring, and attenuation/ground motion analysis), we evaluate the per-
194 formance of the algorithm over a range of metrics: 1) signal-to-noise ratios, 2) surface wave dispersion, 3) convergence of
195 short-term stacks to the long-term stack, 4) transient phase changes, 5) peak amplitudes of ballistic phases, and 6) computa-
196 tional expense. We compare the methods below according to each metric. It is worth noting that there are multiple parameters
197 that can be tuned for each stacking method, though we only focus on the most commonly used or suggested parameters in this
198 study. In Section 5, we discuss the choice of stacking methods for different categories of applications using NCFs.

199 4.1 Signal-to-noise ratios

200 We use the SNR of the ballistic phase as a proxy for the quality of the NCF stack. In this study, we define the SNR, R , as

$$R = \left(\frac{\text{rms}(|A_{\text{signal}}|)}{\text{rms}(|A_{\text{noise}}|)} \right)^2, \quad (6)$$

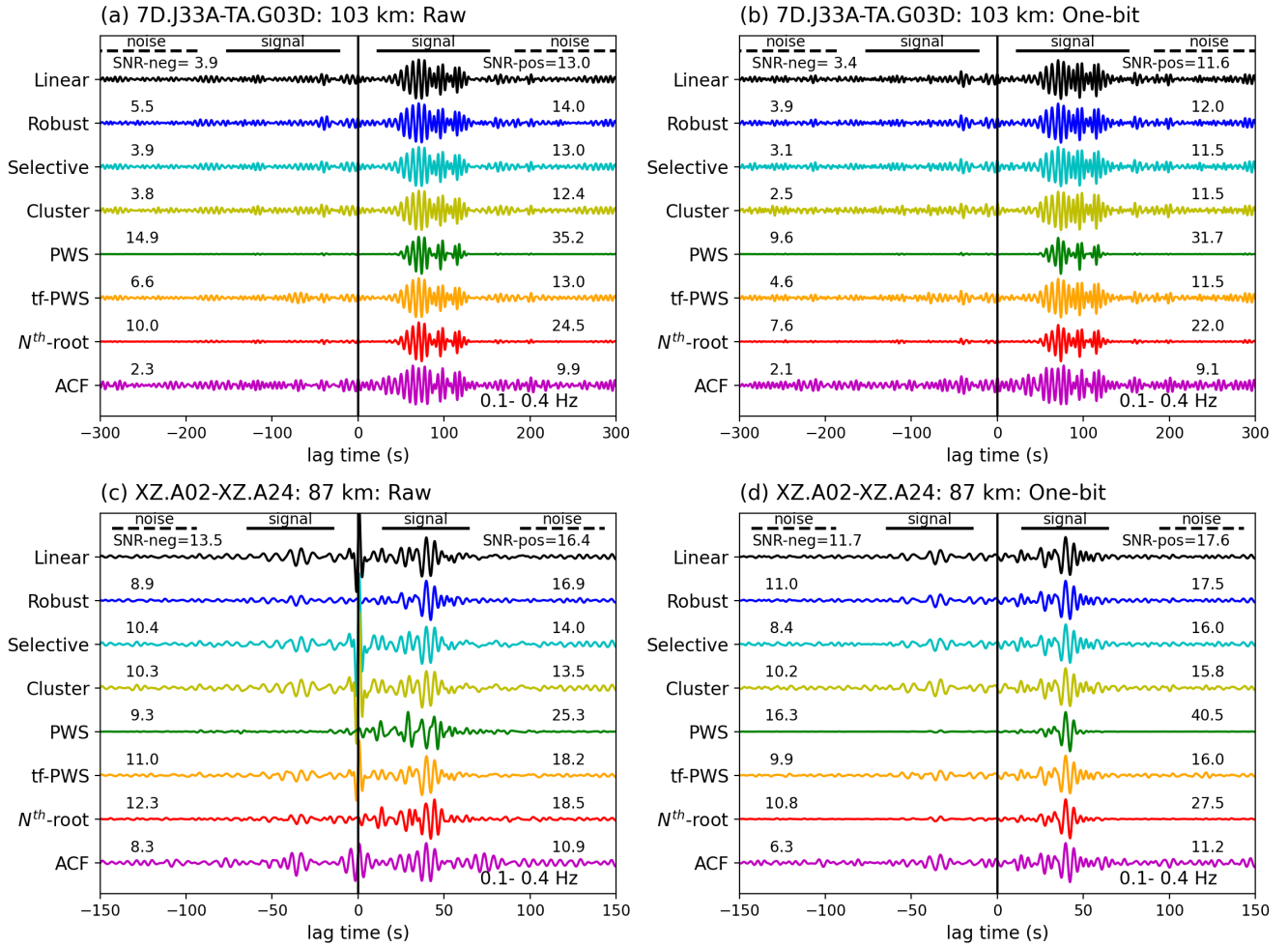


Figure 3. Examples of the stacked NCFs between station pairs (a-b) 7D.J33A-TA.G03D and (c-d) XZ.A02-XZ.A24, using different methods. The left panels are the stacking results for Raw NCFs and the right panels are the stacking results for One-bit NCFs. All NCFs are filtered at 0.1-0.4 Hz after stacking. The stacking algorithm is labeled on the left of each panel. The SNR in decibel (Equation 7) is indicated above each trace on each side of the correlations. The thick solid and dashed lines mark the starts and ends of the signal and noise windows, respectively.

201 where $rms()$ is the root-mean-square operator, $|A_{\text{signal}}|$ are the absolute amplitudes within the signal window, and $|A_{\text{noise}}|$
 202 are the absolute amplitudes within the noise window. For the NCFs from amphibious station pairs (Figs 3a-b, 4, and 6), the
 203 signal window is defined by a fast wave traveling at 4.5 km/s, a slow wave traveling at 2 km/s, and we add 100 s to the end
 204 of the window. For OBS station pairs (Figs 5 and 7), we use a velocity range of 0.5-1.0 km/s to predict the signal window and
 205 add 60 s after the latest predicted arrival time. For the XZ dataset (Figs 3c-d, 8, and 9), the signal window is defined by waves
 206 traveling between 2 km/s and 3.7 km/s, extending for an additional 20 s. For both datasets, the noise window has the same
 207 length as the signal window with an offset of 30 s after the end of the signal window. Considering the relatively large dynamic
 208 range of the computed SNRs, we convert the ratios to decibels for all examples in this paper to assist the comparison, with

$$SNR = 10 \log_{10} R. \quad (7)$$

209 We observe notable variations in the SNRs of the ballistic phases retrieved using different stacking methods. From the

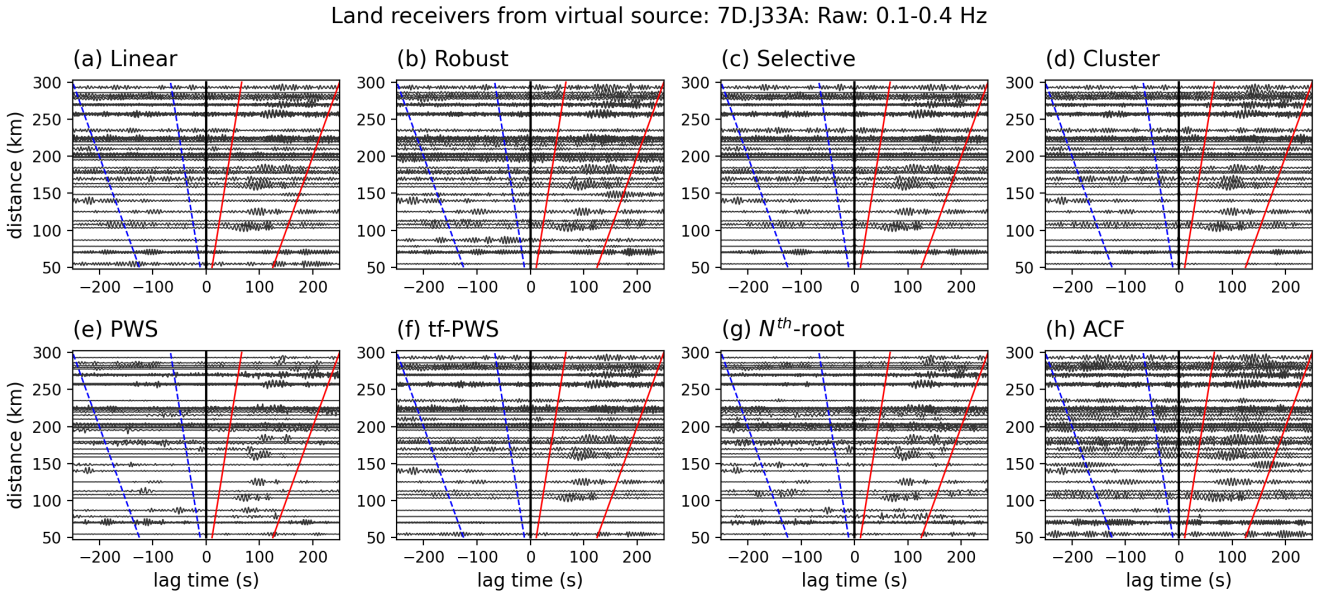


Figure 4. Stacked Raw NCFs of the Cascadia amphibious array from 7D.J33A to other land receivers using different stacking methods, filtered at 0.1-0.4 Hz. (a-h) The results using Linear, Robust, Selective, Cluster, PWS, tf-PWS, N^{th} -root, and ACF stacking methods, respectively. The red solid lines and the blue dashed lines outline the positive-lag signal window and the negative-lag signal window, respectively, used to compute the SNR in Fig. 10. The signal and noise windows are determined with the same method as in Fig. 3a-b. See Fig. 1 for station locations.

210 single-pair examples (Fig. 3), the ballistic phases are most prominent on the positive lags from all stacking results, with
 211 relatively weaker phases on the negative lags, shown as lower SNRs overall. For the Cascadia amphibious station pair, the
 212 SNRs range from 9.9 to 35.2 for the Raw NCFs and 9.1-31.7 for the One-bit NCFs (Fig. 3a-b). For the XZ station pair, the

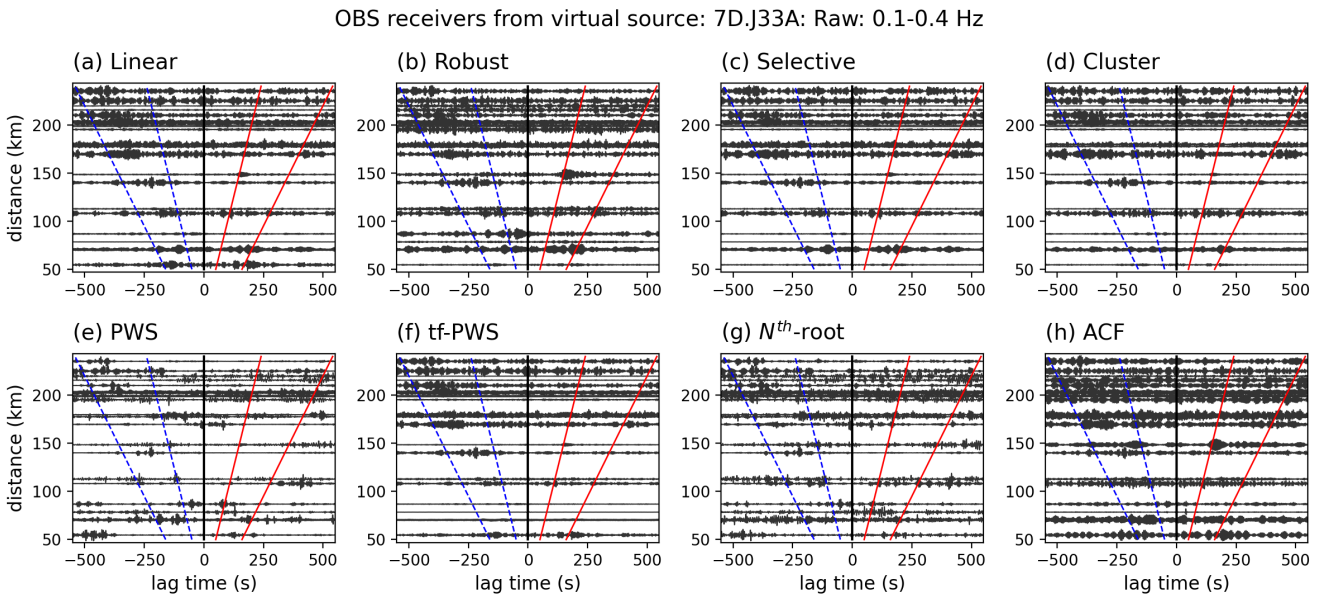


Figure 5. Same as Fig. 4 but for NCFs from 7D.J33A to other OBS receivers. To contain the visually identified ballistic phases from these OBS station pairs, we use a different velocity range (0.5-1.0 km/s) here to predict the signal window of the weakly coherent signals. We extend the window for an additional 60 s after the latest predicted arrival. See Fig. 1 for locations of the OBS receivers.

Land receivers from virtual source: 7D.J33A: One-bit: 0.1-0.4 Hz

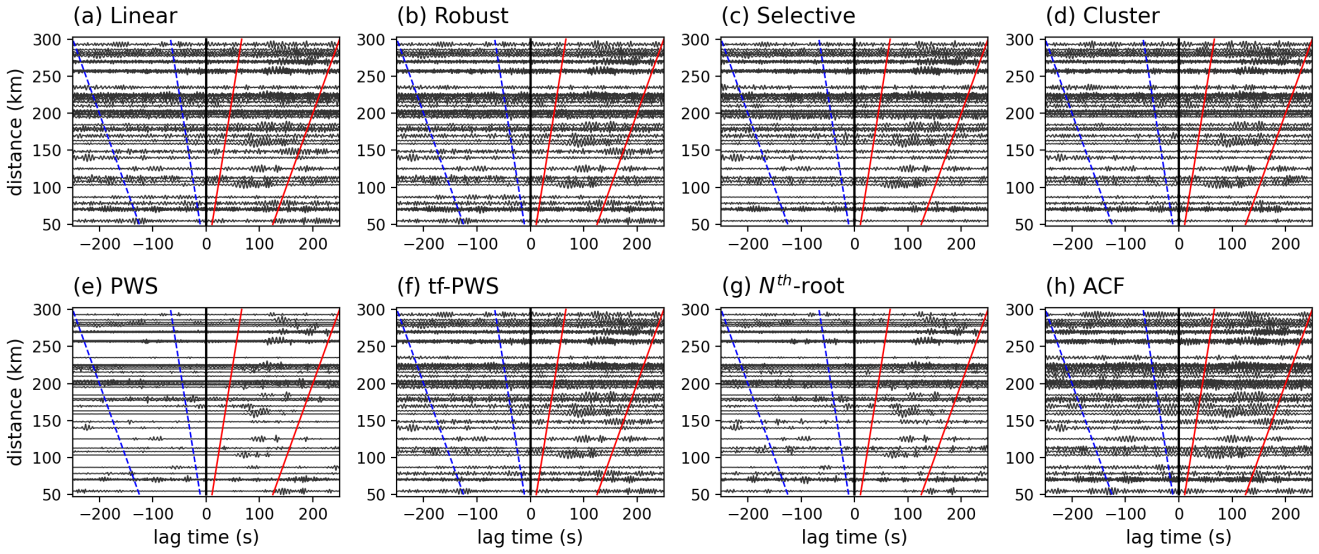


Figure 6. Same as Fig. 4 but for One-bit NCFs.

213 SNRs range from 10.9 to 25.3 for the Raw NCFs and 11.2-40.5 for the One-bit NCFs (Fig. 3c-d). For all datasets, the highest
 214 SNRs are achieved with the PWS method, while the ACF method produces the lowest SNRs. The stacking results using the
 215 N^{th} -root method also show relatively high SNRs. The SNRs of other stacking results are at a comparable level.

216 The stacking results of all station pairs from the same virtual source provide a more holistic comparison of the performance
 217 of different methods (Figs 4-9). We use the mean SNRs across all station pairs to quantify the comparison of stacks with
 218 different methods (Fig. 10). From the visual inspection of the move-out plots (time-lags vs. inter-station distances), the stacks
 219 of Raw (Figs 4 and 8) and One-bit (Figs 6 and 9) NCFs have comparable quality in overall for both the Amphibious and the

OBS receivers from virtual source: 7D.J33A: One-bit: 0.1-0.4 Hz

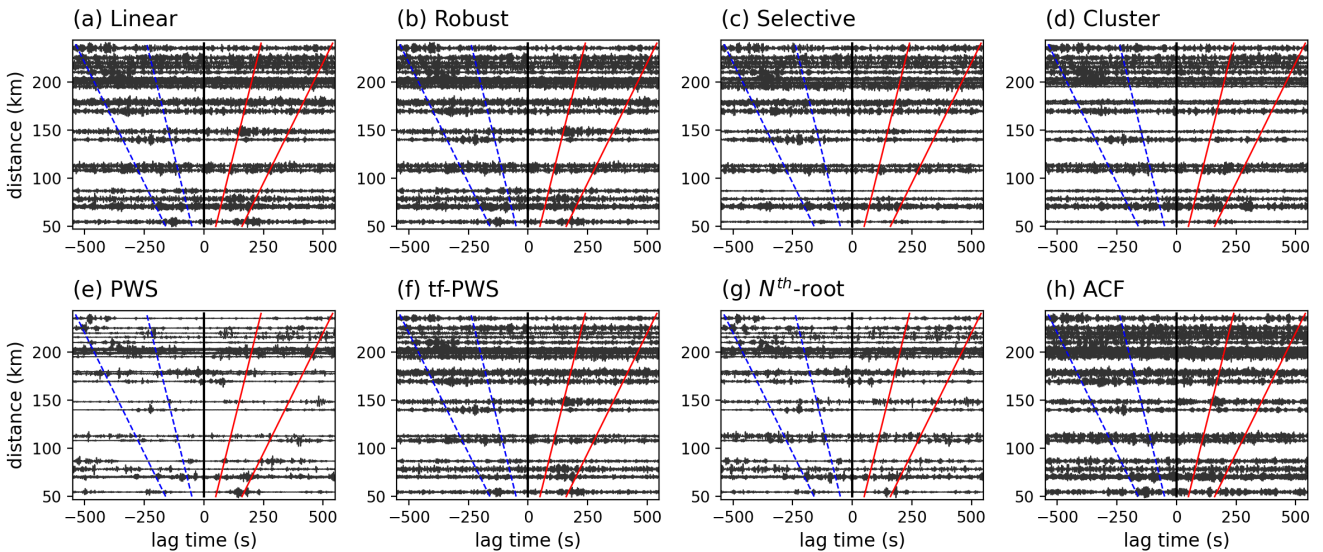


Figure 7. Same as Fig. 5 but for One-bit NCFs.

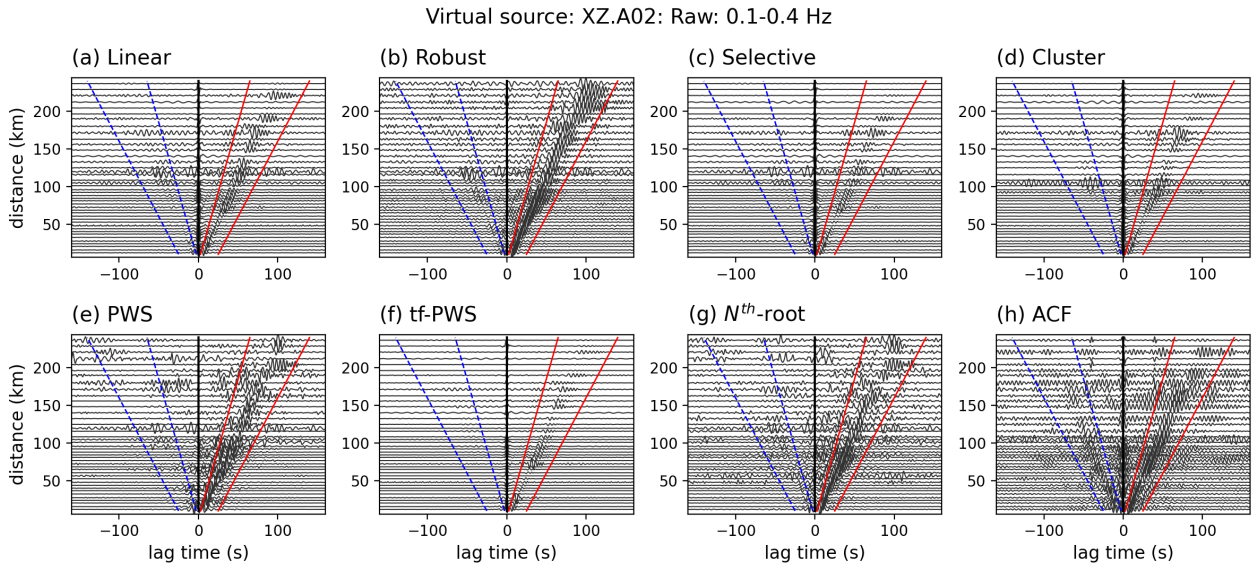


Figure 8. Stacked Raw NCFs between the XZ linear array stations from XZ.A02 to other receivers, filtered at 0.1-0.4 Hz. (a-h) The results using Linear, Robust, Selective, Cluster, PWS, tf-PWS, N^{th} -root, and ACF stacking methods, respectively. The red solid lines and the blue dashed lines outline the positive signal window and the negative signal window, respectively, used to compute the SNR in Fig. 10. The signal and noise windows are determined with the same method as in Fig. 3c-d. See Fig. 1 for station locations.

220 XZ datasets. This is also evident from the comparable mean SNR values of the two pre-processing methods (Fig. 10). For the
 221 Cascadia Amphibious dataset, most of the NCFs from the OBS receivers are relatively noisy (Figs 5 and 7), with mean SNRs
 222 lower than those from the onshore receivers (Fig. 10a-b). This may result from the contamination of tilt and compliance noise
 223 at most OBS stations, a well known problem in offshore data (Tian and Ritzwoller 2017). Most of the stacked XZ NCFs show
 224 clear ballistic phases (Fig. 8-9), with much higher mean SNRs than those of the Amphibious dataset (Fig. 10). In all examples
 225 with land receivers, the ballistic phases are dominantly visible at positive lag times, representing surface waves propagating

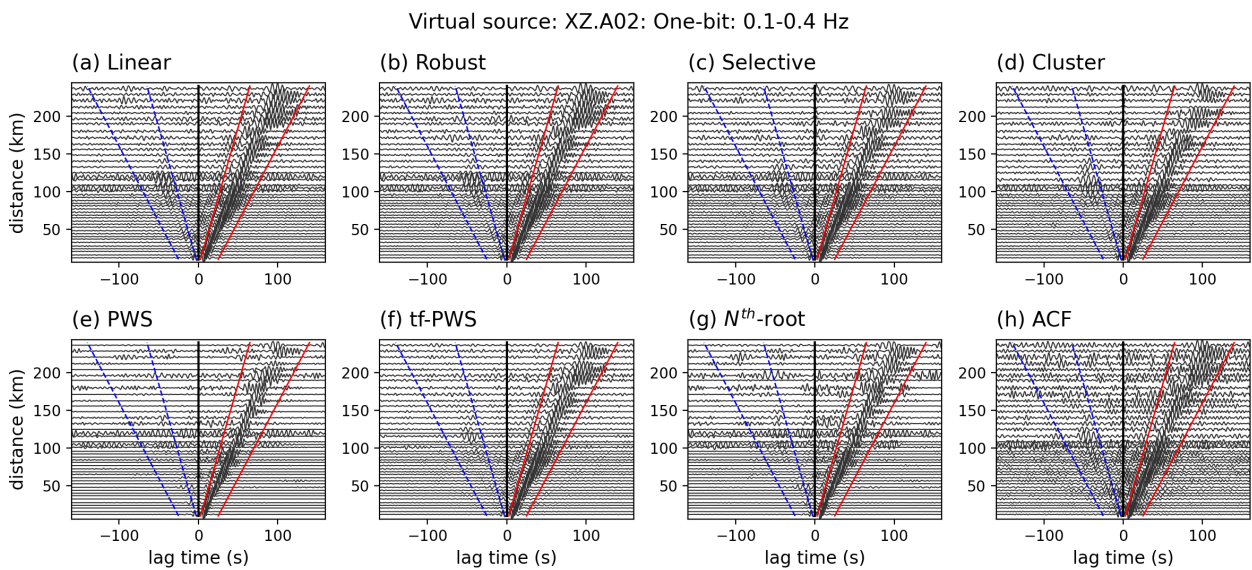


Figure 9. Same as Fig. 8 but for One-bit NCFs.

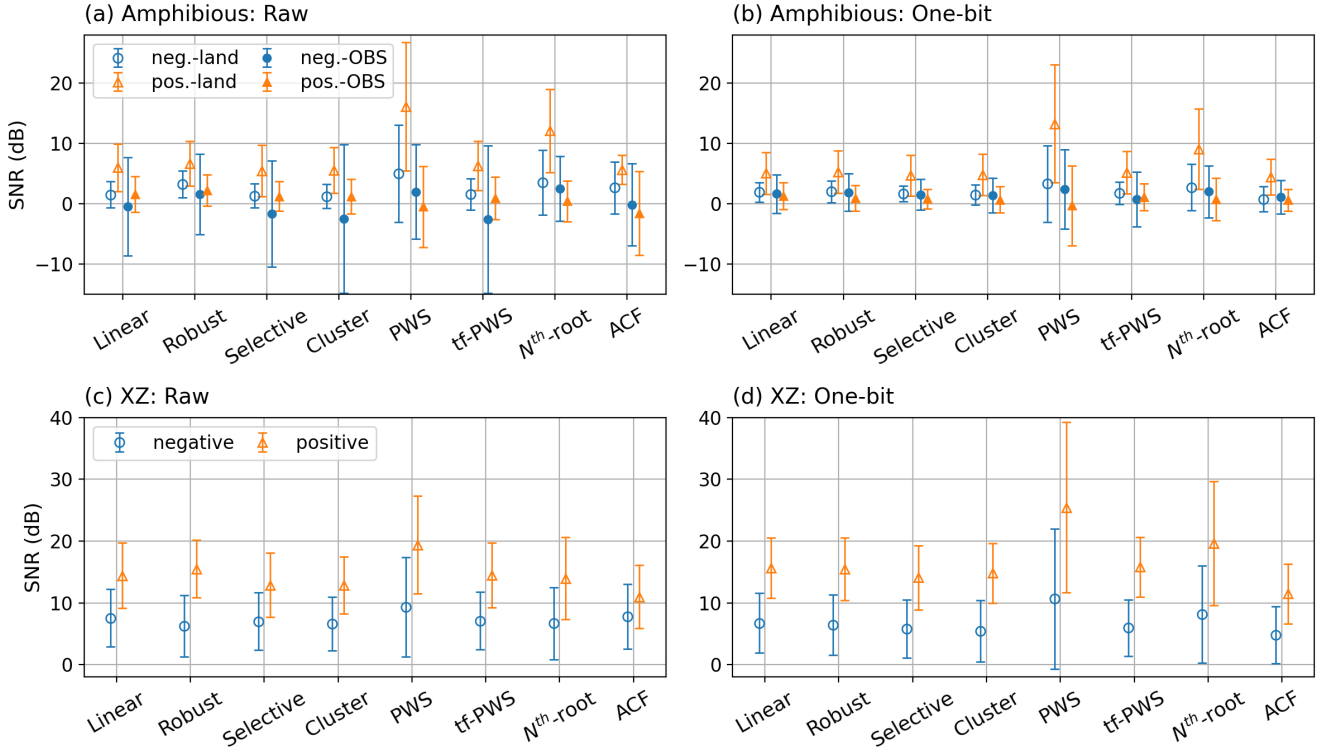


Figure 10. Comparison between the mean signal-to-noise ratios (SNRs) for the NCFs shown in Figs 4-9. (a-b) Mean SNRs for the Cascadia amphibious array Raw and One-bit NCFs, respectively. The SNRs for the land (open circles and triangles) and OBS (dots and filled triangles) stations are plotted separately. (c-d) Results for the XZ linear array NCFs from Raw and One-bit NCFs, respectively. The error bars show the standard deviations of the SNRs.

226 away from the virtual sources, which we focus on for the following description. For all four datasets (land receivers only for
 227 the Amphibious NCFs), the PWS method produces the highest SNRs, while the standard deviation of the SNRs is also the
 228 largest. For the Cascadia Amphibious NCFs (Fig. 10a-b), N^{th} -root stacking yields the second highest SNRs, while the SNRs
 229 of other stacking results are at a comparable level of 0-10 for both the Raw and One-bit NCFs. For the XZ NCFs (Fig. 10c-d),
 230 the lowest SNRs are observed with ACF stacking, though the ballistic phases are still clearly retrieved (Figs 8h and 9h).

231 4.2 Surface wave dispersion

232 Surface waves are dispersive, which means that the seismic wavespeed depends on the frequency of the wave. Specifically,
 233 lower frequency (longer period) waves travel faster than higher frequency (shorter period) waves and are more sensitive to
 234 greater depths. This frequency-depth characteristic makes surface waves a popular choice for elastic and anelastic seismic
 235 tomography. Preserving the surface wave dispersion in the stacked NCFs is, therefore, one of the critical metrics to evaluate the
 236 performance of different stacking methods. We assess this performance by extracting the dispersion curve with peak amplitudes
 237 from individual station pairs and examining their statistical behaviors.

238 We follow the procedure described in Yao et al. (2006) to extract the phase velocity dispersion curve. The steps of the
 239 algorithm are: 1) apply a narrow-band filter to the stacked NCF and transform to a 2D time-frequency space, 2) detect the

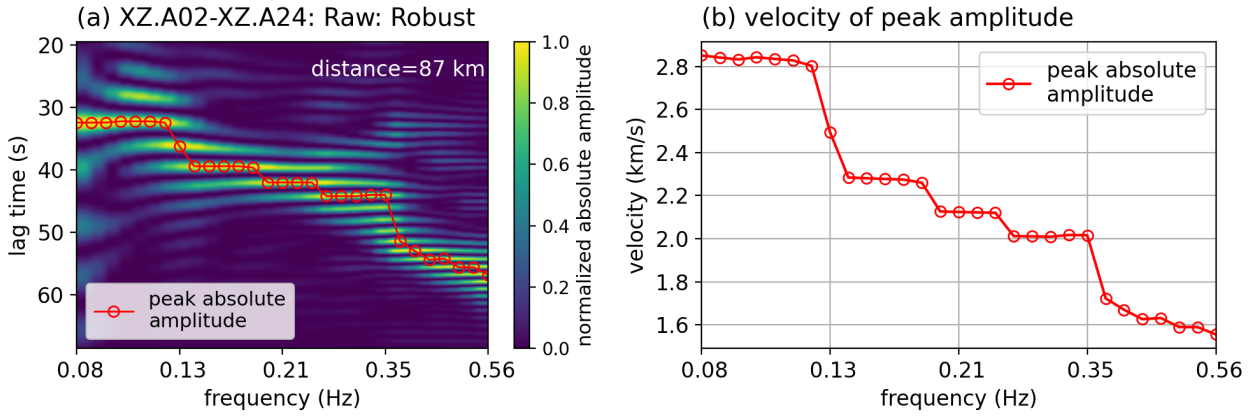


Figure 11. Example of extracting the phase-velocity dispersion curve. The red circles mark the time and velocity measurements. (a) Time-frequency representation of the Robust-stacked Raw NCF for the station pair XZ.A02-XZ.A24, normalized at each frequency. (b) Dispersion curve generated from (a) with the given inter-station distance (i.e., 87 km for this example).

240 arrival time of the peak absolute amplitude at each frequency, and 3) convert the peak arrival time to velocity with the inter-
 241 station distance. We use all individual station pairs to increase the sample size in our statistical comparison.

242 We filter the NCFs with narrow-band filters before searching for the peak arrival times within the predicted signal window.
 243 For each individual NCF, the window length is the same for all frequencies. To sample enough data at the low-frequency range,
 244 we use non-linear frequency increments, with smaller steps for lower frequencies and gradually increasing steps at higher

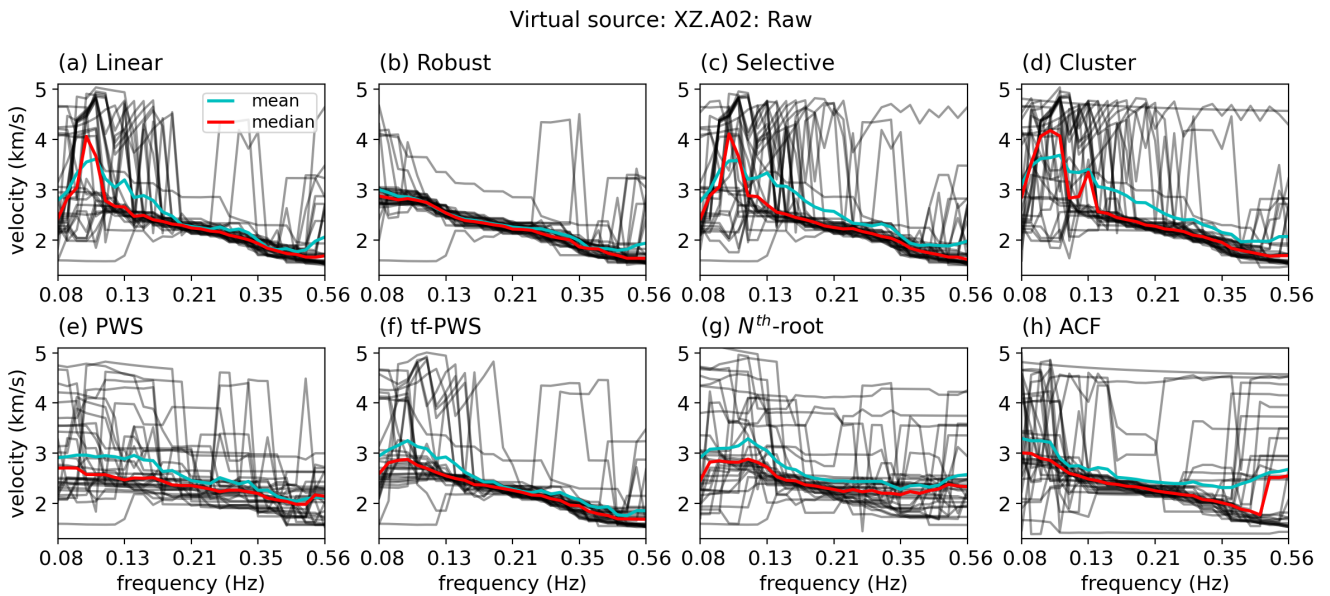


Figure 12. Dispersion curves of the ballistic phases extracted from the Raw NCFs between the virtual source at XZ.A02 and other receivers, as shown in Fig. 8. (a-h) Results from the stacks using Linear, Robust, Selective, Cluster, PWS, tf-PWS, N^{th} -root, and ACF stacking methods, respectively. Black lines are measurements from all individual station pairs using the procedure illustrated in Fig. 11. Cyan and red lines are the mean and median of all measurements at a given frequency.

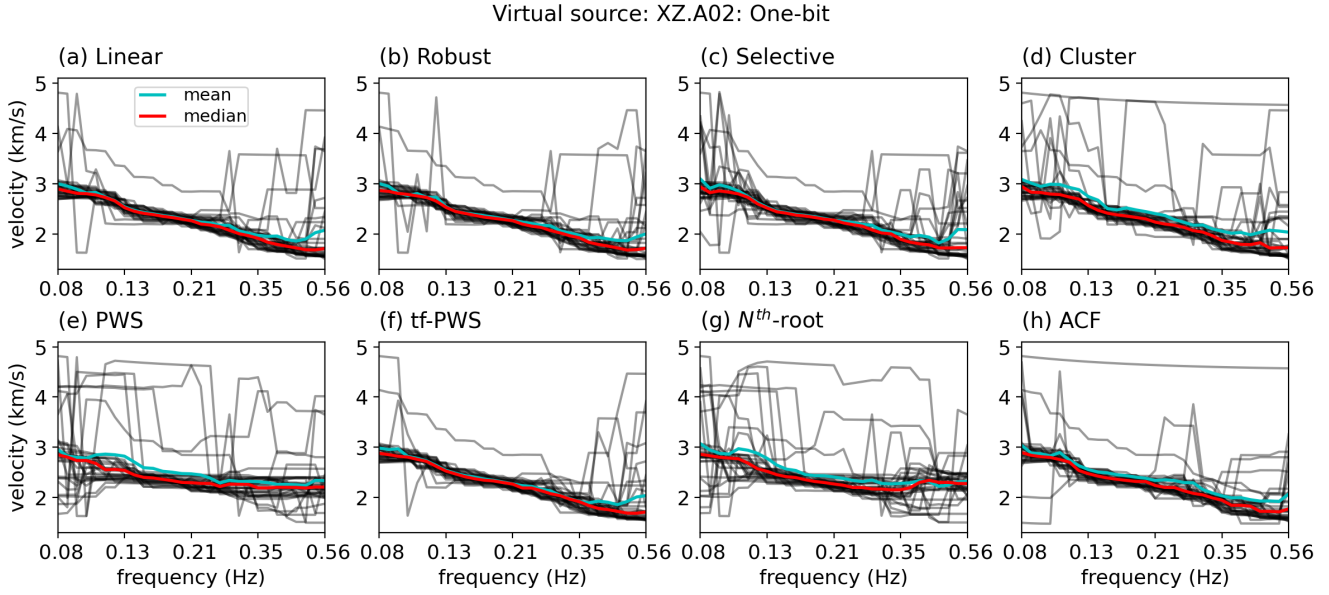


Figure 13. Same as Fig. 12 but for stacked One-bit NCFs as shown in Fig. 9.

245 frequencies. The frequency vector, \mathbf{f} , is computed as

$$\begin{cases} \mathbf{f} = (2^{\mathbf{T}_L})^{-1} \\ \mathbf{T}_L = [\log_2(a_1 T_{min}), \log_2(a_2 T_{max}), dT_L] \end{cases}, \quad (8)$$

246 where \mathbf{T}_L is the period vector in \log_2 space from $\log_2(a_1 T_{min})$ to $\log_2(a_2 T_{max})$ with a step of dT_L , $T_{min} = 1/f_{max}$ and
 247 $T_{max} = 1/f_{min}$ are the desired period range with f_{min} and f_{max} being the corresponding frequency range, and a_1 and a_2 are
 248 the scaling factors to extend the period range to cover the desired frequency range. The examples shown here use $f_{min}=0.08$
 249 Hz, $f_{max}=0.6$ Hz, $dT_L=0.1$, $a_1=0.1$, and $a_2=2$. Each narrow filtering band spans across 10 frequency steps, with the center
 250 frequency shown for our analyses.

251 In our study, we focus only on the positive lag of the NCF and in a time window defined as a wave traveling between 2

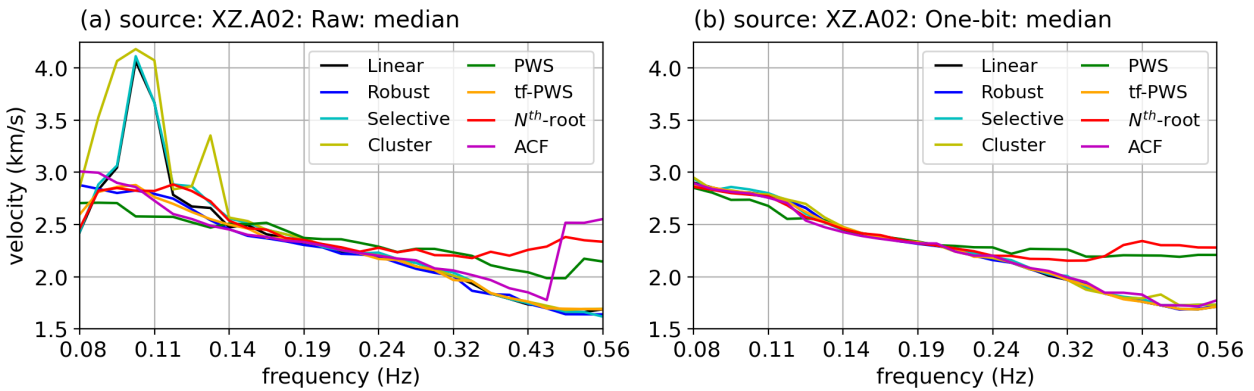


Figure 14. Comparison of median dispersion curves from XZ.A02 to other receivers for (a) Raw and (b) One-bit NCF stacks. The raw measurements are shown in Figs 12-13.

252 km/s and 4.5 km/s, adding 20 s at the end of the window. Following Yao et al. (2006), we subtract $T/8$ from the peak arrival
 253 time, where T is the corresponding period, and then compute the phase velocity. We show one example of the robust stack
 254 from the station pair XZ.A02-XZ.A24 that has an inter-station spacing of 87 km. We show the travel-time measurements in the
 255 time-frequency representation in Fig. 11a and the corresponding phase velocity curve generated by the algorithm as illustrated
 256 in Fig. 11b.

257 We apply this procedure to all station pairs with the common virtual source XZ.A02. To satisfy the far-field approximation,
 258 we only analyze the results from station pairs with inter-station distances of ≥ 56 km, which is the maximum wavelength at
 259 0.08 Hz with a velocity of 4.5 km/s. We construct the dispersion curves using different stacking methods for both Raw and
 260 One-bit NCFs (Figs 12-13). There are consistent signals at frequencies above about 0.1 Hz, though we also observe noticeable
 261 jumps in the individual dispersion curves. The jumps may be attributed to cycle skipping in the travel-time measurements. We
 262 measure the mean and median value among all station pairs at each frequency. The median is a more robust measure of the
 263 dispersion curves, given the unstable jumps in the curves.

264 The overall dispersion shows a decrease of the phase velocity with increasing frequency, from about 3 km/s at 0.08 Hz
 265 to about 1.7-1.8 km/s at 0.56 Hz (Figs 13 and 14b). However, the overall quality of the results varies substantially between
 266 methods and pre-processing techniques. The dispersion curves for the Raw NCFs vary significantly among the different stack-
 267 ing methods (Fig. 12). The dispersion extracted from the Linear, Selective, Cluster, PWS, and ACF stacking methods is highly
 268 variable (Fig. 12a, c, d, e, and h). Only the Robust stacking method provides stable dispersion results for Raw NCFs (Fig. 14a).
 269 In comparison, the dispersion curves for the One-bit NCFs are relatively more stable (Fig. 13), which is probably why the
 270 One-bit pre-processing is preferred in most ambient-noise tomography.

271 Generally, all stacking methods successfully preserve the overall dispersion patterns between 0.14 Hz and 0.24 Hz (Fig.
 272 14) for both pre-processing techniques. The median dispersion curves from the Linear, Selective, Cluster, and tf-PWS are
 273 similar to that from the Robust stacking result at frequencies above about 0.14 Hz (Fig. 14a). At lower frequencies (< 0.14 Hz),
 274 the medians of the Linear, Selective, and Cluster results show anomalously high velocities comparing to other methods. For
 275 both Raw and One-bit NCFs, the PWS and N^{th} -root methods seem to flatten the dispersion at higher frequencies, resulting
 276 in notably higher velocities than other methods at frequencies above 0.24 Hz (Fig. 14). This means that the wave dispersion
 277 information in the time series is lost with these methods at relatively high frequencies.

278 4.3 Convergence of short-term stacks to the long-term stack

279 In measuring the temporal changes associated with the elastic properties of the crust, we often stack a subset of the short-term
 280 NCFs over an intermediate time period (e.g., F. Brenguier et al. 2008; Clements and Denolle 2018; Donaldson et al. 2019;
 281 Hadzivoannou et al. 2011; Olivier et al. 2019; Seats et al. 2012; Yuan et al. 2021). The time needed to reach convergence limits
 282 the temporal resolution of the monitoring of the change in elastic properties. Here, we quantify the *rate of convergence* as the
 283 time duration of NCFs needed to achieve a certain threshold of the correlation coefficient between the stack of the subset NCFs

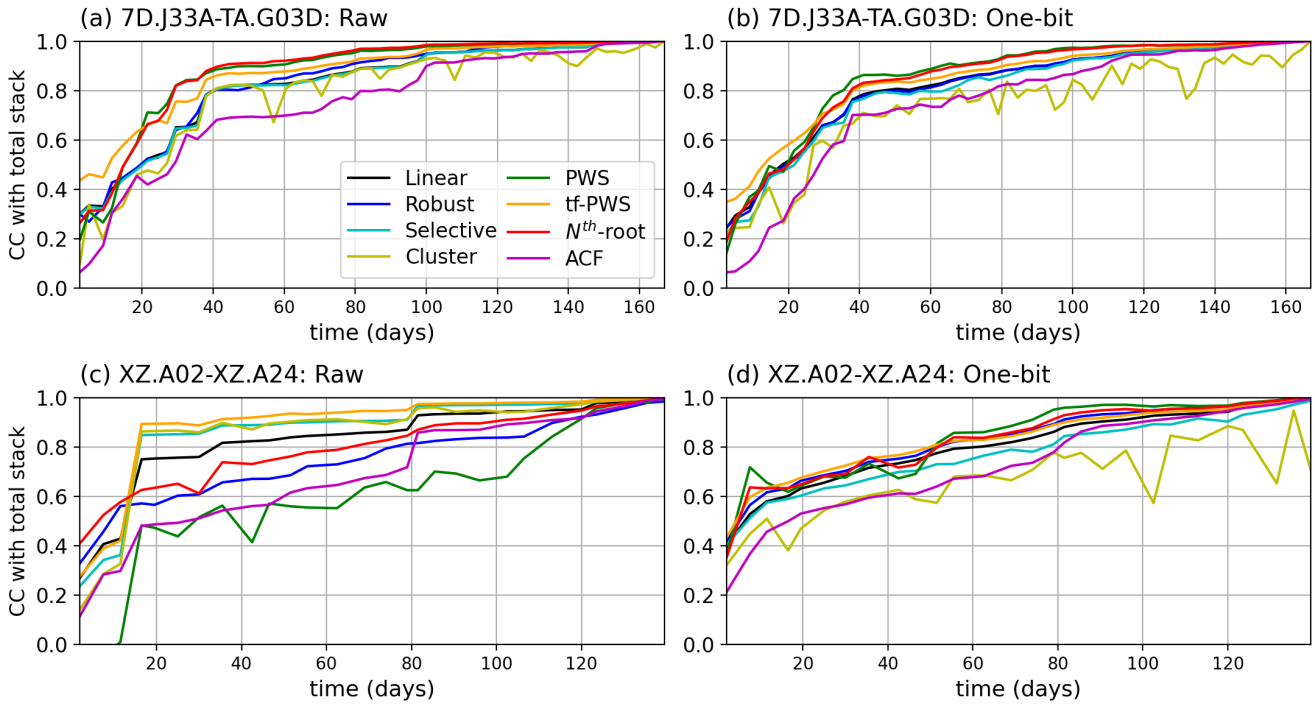


Figure 15. Convergence to long-term stacks with the increasing number of NCFs, shown as the equivalent time span of NCFs in days. (a-b) Correlation coefficients (CC) between the progressive stacking results and the stacks over the entire time period for Raw and One-bit NCFs between station pair 7D.J33A-TA.G03D. The pre-stack NCFs are shown in Fig. 2a-b. We only use NCFs before 4/1/2012 for the convergence analysis to exclude the much noisier data in later dates. All stacks are filtered at 0.1-0.4 Hz. (c-d) Same as (a) and (b) but for the XZ station pair XZ.A02-XZ.A24. The pre-stack NCFs are shown in Fig. 2c-d. We use all NCFs for this station pair.

284 and the reference stack of NCFs over the entire period. We compute the correlation coefficient between the reference stack and
 285 the stack of a progressively growing subset of NCFs ordered by date and time with an increment of 5 NCFs (Fig. 15).

286 The rate of convergence varies among methods (Fig. 15). Overall, the PWS, tf-PWS, and N^{th} -root stacking results have
 287 the fastest convergence to the reference stack (Fig. 15a, b, and d), except for the Raw NCFs from the XZ station pair (Fig.
 288 15c) where the PWS method converges the slowest. The ACF stacking result converges the slowest for the Raw NCFs of the
 289 Cascadia amphibious station pair (Fig. 15a). The Cluster stacking method converges the slowest for the One-bit NCFs from
 290 both station pairs (Fig. 15b and d), though it shows a fast convergence rate for the Raw NCFs of the XZ station par (Fig. 15c).
 291 The strong fluctuation of the results using Cluster stacking may be due to the fact that k-means clustering method involves
 292 some random processes in assigning the clusters. Most stacking results achieve high (≥ 0.7) correlation coefficients with more
 293 than about 35 days (Fig. 15a-b). For the XZ NCFs to achieve a similar correlation coefficient, it takes about 50 days (Fig.
 294 15c-d). From the results shown here, the rate of converge depends strongly on the specific dataset and the quality of individual
 295 short-term NCFs.

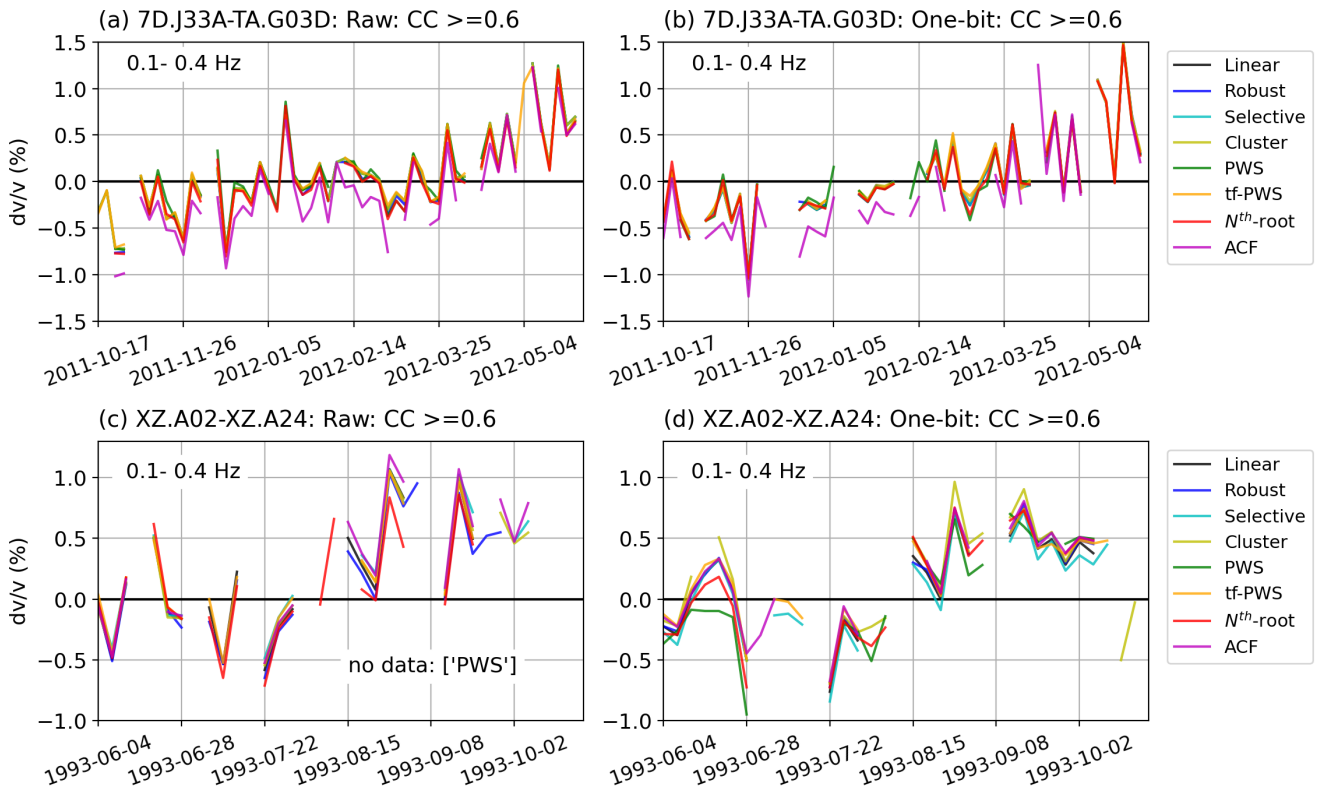


Figure 16. Transient velocity changes (dv/v) using the trace stretching method measured from NCFs from (a) 7D.J33A-TA.G03D and (b) XZ.A02-XZ.A24. The pre-stack short-term NCFs and the measuring windows are shown in Fig. 2. We use coda waves for the amphibious station pair (7D.J33A-TA.G03D) and ballistic phases for the XZ station pair (XZ.A02-XZ.A24). The coda waves for the XZ station pair (both Raw and One-bit NCFs) are not coherent and produce unstable dv/v measurements, regardless of the stacking method used. For 7D.J33A-TA.G03D, we only analyze the NCFs before 6/2/2012, where we have clear coda phases on most of the NCFs. We sub-stack the NCFs over 96 hours (4 days) for all station pairs. We only plot dv/v results with after-stretching correlation coefficient (CC) of ≥ 0.6 .

296 4.4 Transient phase changes

297 Seismic monitoring using ambient noise interferometry relies on the phase difference of seismic waves measured at different
 298 times (e.g., F. Brenguier et al. 2008; Clements and Denolle 2018; Donaldson et al. 2019; Hadziioannou et al. 2011; Olivier
 299 et al. 2019; Seats et al. 2012; Yuan et al. 2021). We analyze how transient phase changes are preserved with different stacking
 300 methods by measuring the velocity changes with time (dv/v). We utilize the trace stretching method (e.g., Florent Brenguier
 301 et al. 2008; Lobkis and Weaver 2003; A. Obermann et al. 2014; Yuan et al. 2021) to measure the dv/v between the two example
 302 station pairs: 7D.J33A-TA.G03D and XZ.A02-XZ.A24 (Fig. 16). The trace stretching method estimates dv/v by maximizing
 303 the correlation of the individual NCF with the reference trace through linearly stretching or squeezing the waveform within
 304 the specified time window. The Python function for trace stretching is built in the *SeisGo* interface (X. Yang et al. 2022a). For
 305 all results shown in Fig. 16, we measure the velocity changes in the frequency range of 0.1-0.4 Hz. For all datasets, we use a
 306 sub-stacking window length of 96 hours (4 days). The measuring windows are 86-106 s for 7D.J33A-TA.G03D to capture the

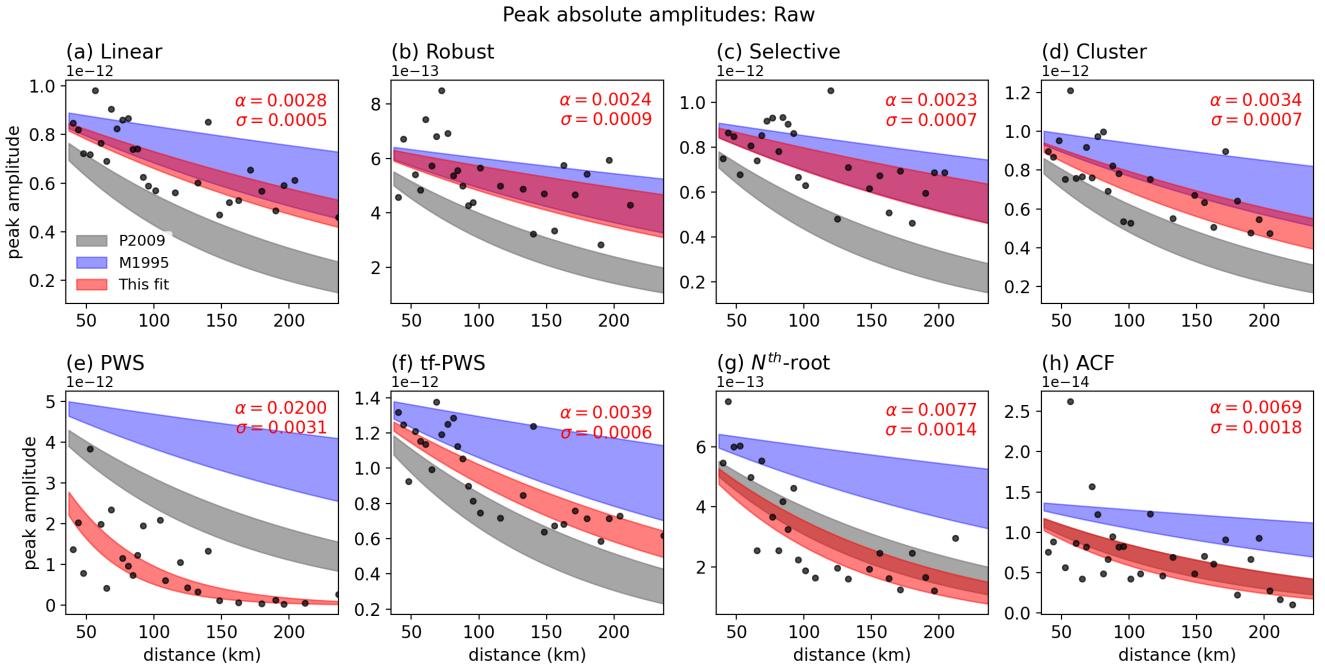


Figure 17. Peak absolute amplitudes of the positive lags of the XZ Raw NCFs within the predicted ballistic arrival windows computed using a velocity range of 2-3.7 km/s and corrected by \sqrt{D} , D is the inter-station distance. In each panel, we only show the attenuation parameter, α , and its standard deviation, σ . The exponential fit from this study is shown as the red shaded area. For reference, we also show the amplitude decay estimated based on the attenuation parameters from Prieto et al. (2009) (P2009; $\alpha=0.0064\pm 0.0013$; gray shaded area) and Mitchell (1995) (M1995; $\alpha=0.002\pm 0.001$; blue shaded area). See Fig. 8 for the moveout plots of the stacked NCFs.

307 coda waves and 29-49 s for XZ.A02-XZ.A24 containing the ballistic phases. The dv/v measuring windows for both datasets
 308 are marked in Fig. 2.

309 For each station pair, different stacking methods produce very similar patterns of transient velocity changes over the ob-
 310 servational periods (Fig. 16). An exception is the dv/v measurements from the PWS stacking result of the Raw XZ NCFs, with
 311 stronger variations and much lower after-stretching correlation coefficient compared to other stacking results. After applying
 312 the geq 0.6 threshold for after-stretching correlation coefficient in plotting Fig. 16, there is no PWS measurements left. For
 313 7D.J33A-TA.G03D, a general increase in seismic velocity from -0.5% to 0.5% is observed from both Raw and One-bit NCFs
 314 using all stacking methods (Fig. 16a-b). For XZ.A02-XZ.A24, the dv/v is fluctuating between -0.5% and 0.5% from June to
 315 July of 1993 (Fig. 16c-d). From August 1993 to the end of the observational period, the dv/v varies between 0% and 1% (Fig.
 316 16c-d). While we do not intend to interpret these dv/v measurements, we note the great similarity of the measurements across
 317 methods. All stacking methods show comparable results in preserving the transient phase differences for coda waves from both
 318 Raw and One-bit NCFs and the ballistic phases from One-bit NCFs. The PWS method fails with this metric for ballistic phases
 319 from the XZ Raw NCFs.

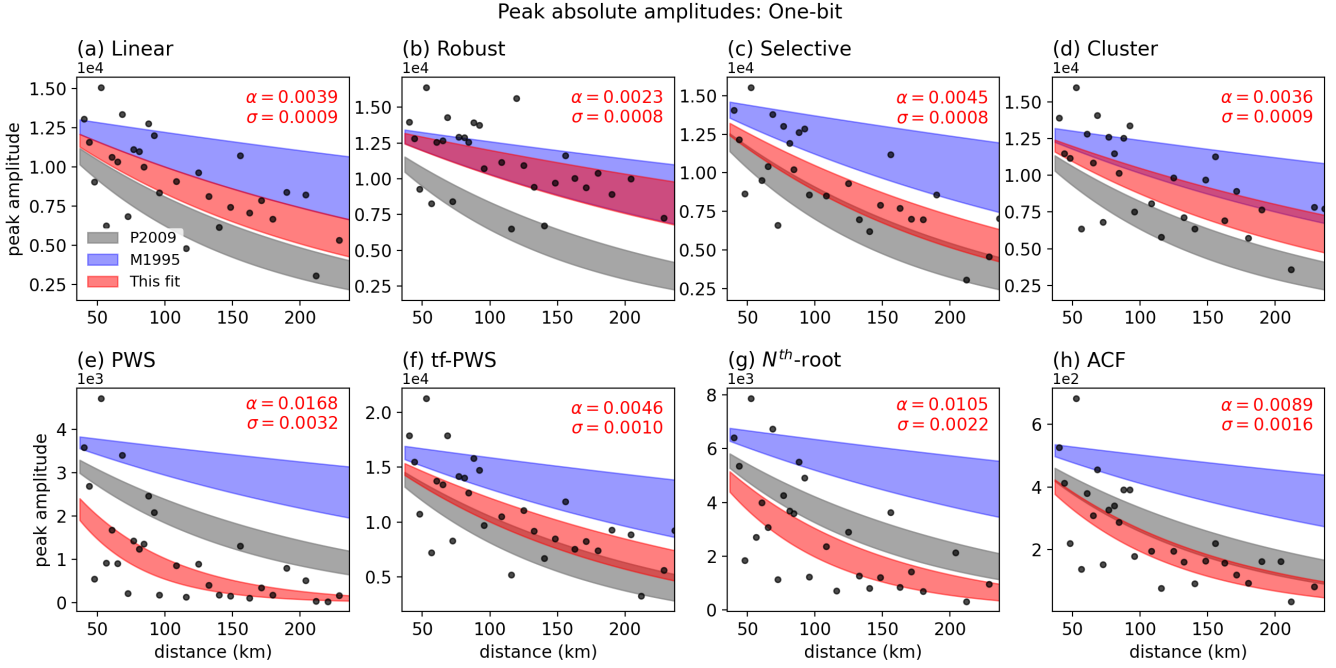


Figure 18. Same as Fig. 17 but for measurements from the XZ One-bit NCFs. See Fig. 9 for the moveout plots of the stacked NCFs.

320 4.5 Peak amplitudes of ballistic phases

321 Important information about the Earth anelastic structure can be retrieved from the relative amplitudes of NCFs. Here, we
 322 focus on the amplitude decay with distance and ignore the spatial variations in relative amplitudes that are subject to additional
 323 uncertainties. The NCFs chosen in this example are the same as in Figs 8 and 9, filtered at 0.1-0.4 Hz. We measure the peak
 324 absolute amplitudes of the predicted ballistic waves within the time windows computed with a velocity range of 2-3.7 km/s
 325 (Figs 8 and 9). The XZ broadband network is an East-West trending linear array in central Oregon, United States (Fig. 1). It is
 326 located at the active Cascadia convergent margin, spanning from the Cascadia Range in the East to the coastal mountains in the
 327 West. Considering that noise is dominantly generated by the oceanic microseisms (e.g., Webb 1998; Y. Yang and Ritzwoller
 328 2008), the XZ linear array provides an appropriate dataset for analyzing the attenuation of surface waves extracted from
 329 NCFs, minimizing the azimuthal dependence of noise sources. In this work, we only aim to compare the stability of the
 330 relative amplitude information with different stacking methods and do not intend to advocate for an estimate of attenuation,
 331 which might still depend on the distribution of noise sources (Laurent Stehly and Boué 2017). Since the microseismic noise is
 332 dominantly generated in the ocean and propagates eastward from the coast where the virtual source XZ.A02 is located (Fig. 1),
 333 we only show the attenuation measurements from the positive lags.

334 Assuming that the main signals are fundamental-mode surface waves, the maximum absolute amplitude of the stacked
 335 NCFs (Figs 17-18) decay with distance:

$$A(D) = A_0/\sqrt{D} \exp(-\alpha D), \quad (9)$$

336 where D is the inter-station distance, A_0 is a reference amplitude at the virtual source, α is a measure of "attenuation" that
 337 can be attributed to intrinsic and scattering attenuation that further reduces the ground motion. To fit α , we correct for the
 338 geometrical spreading by scaling the amplitudes with a factor of \sqrt{D} . The peak absolute amplitudes are then fit to an expo-
 339 nential function $y = e^{-\alpha x}$. We estimate the best fit through least square linear regression of the peak amplitudes in a natural
 340 logarithmic space using the following steps: 1) calculate the natural log peak absolute amplitudes, 2) fit all data points using
 341 a least square linear regression (`scipy.stats.linregress`), 3) correct the data with the best fit model and measure misfit,
 342 4) compute the mean and standard deviation of the misfit, 5) remove the outliers (data points that are more than one standard
 343 deviation away from the mean), and 6) use the remaining subset of the data to repeat step-2 to get the final linear fit parame-
 344 ters. The slope parameter in the linear regression from step-2 is the attenuation factor α . The error in slope estimate given by
 345 `scipy.stats.linregress` is then used as the uncertainty of α , as shown in Figs 17 and 18.

346 We only use subsets of the NCFs in Figs 8 and 9 that have inter-station distances between 37 km, which is the wavelength
 347 of a 0.1 Hz wave traveling at a velocity of 3.7 km/s) and 240 km. The exponential fit, with the uncertainties, from this study is
 348 shown as the red shaded area in Figs 17 and 18. For comparison, we also plot the independent attenuation measurements from
 349 Prieto et al. (2009) ($\alpha=0.0064\pm 0.0013$) for the Los Angeles Basin in southern California using ambient noise NCF filtered at
 350 0.2 Hz and Mitchell (1995) ($\alpha=0.002\pm 0.001$) for active tectonic regions measured at 0.1-0.2 Hz using a global compilation of
 351 earthquake surface waves.

352 One of the most important results is that the decay coefficient α can be measured with all methods and for all pre-processing
 353 techniques. There are, however, great variability (0.0023-0.02 for Raw NCFs and 0.0023-0.0168 for One-bit NCFs; Figs 17-
 354 18). For Raw NCFs (Fig. 17), the attenuation parameters measured from the stacking results using Linear, Robust, Selective,
 355 and Cluster methods are similar to the values by Mitchell (1995). The coefficients using the N^{th} -root and ACF methods are
 356 comparable to that found by Prieto et al. (2009), who used spectral methods to measure attenuation in the Los Angeles basin.
 357 The coefficient from the tf-PWS method falls in-between the values provided by Mitchell (1995) and Prieto et al. (2009). For
 358 the estimates from One-bit NCFs (Fig. 18), the result using the Robust method overlaps the most with the value proposed by
 359 Mitchell (1995). The Linear, Selective, Cluster, and tf-PWS stacking results all fall in-between the values by Mitchell (1995)
 360 and Prieto et al. (2009). The estimates of α from the N^{th} -root and ACF stacks are similar to that used by Prieto et al. (2009).
 361 Compared to the attenuation measurements from the Raw NCFs, the attenuation measurements from the One-bit NCFs seem
 362 to be more sensitive to the choice of stacking methods, shown as larger variations among different methods. For both datasets,
 363 the PWS method tends to overestimate the attenuation factors, α , with much higher values than other methods.

364 4.6 Computational expenses

365 The computational efficiency of different stacking methods varies significantly among different stacking methods, but as ex-
 366 pected does not change between Raw and One bit NCFs. The compute times are estimated from a single core 3.6 GHz Intel

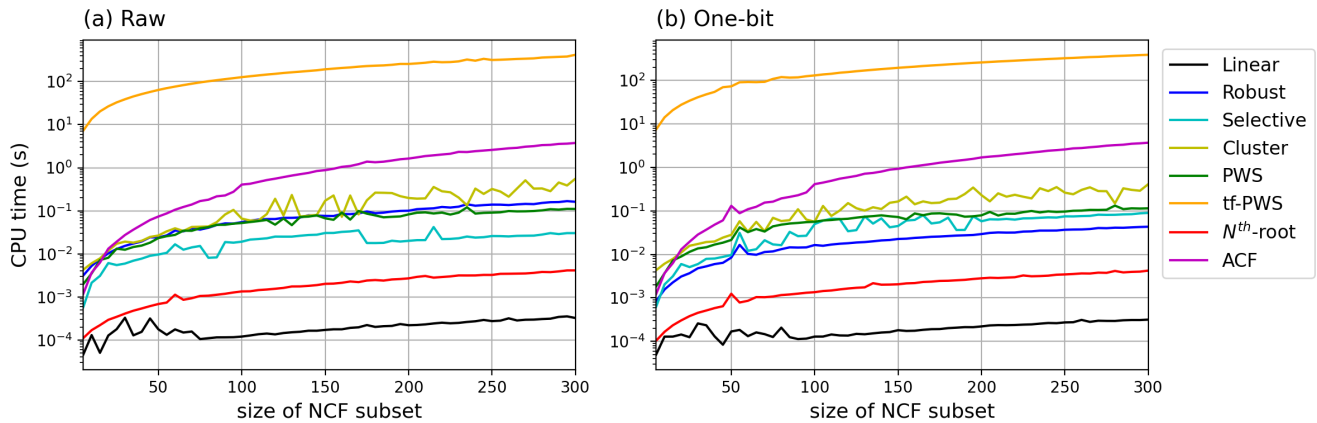


Figure 19. Computing times spent on stacking as a function of the number of NCFs to stack in a 5-step increment for (a) Raw and (b) One-bit NCFs from station pair 7D.J33A-TA.G03D.

367 Core i9 CPU. We compare the compute time spent stacking subsets of the NCFs (with an increment of 5 NCFs) using the
 368 different stacking methods (Fig. 19). The tf-PWS stacking uses the most CPU time while the linear stacking (Linear) is the
 369 fastest method (Fig. 19). Most of the time in tf-PWS is spent on computing the Stockwell transform on individual NCFs. While
 370 our implementation here follows that of the original Stockwell transform, Baig et al. (2009) found a more efficient algorithm
 371 to compute the Stockwell transform. The CPU time tf-PWS takes is about six orders of magnitudes greater than that of the
 372 Linear stacking. For example, tf-PWS takes about 400 seconds to stack 300 NCFs, while the Linear stacking takes 0.0005s.
 373 The ACF stacking method is the second most expensive method in terms of computing time, with about 4 seconds to stack 300
 374 NCFs. This is because the ACF method needs to compute the spectrum of each individual trace as well as the cross-spectrum
 375 in moving windows. The Robust, Selective, and Cluster methods take about 0.02-0.4 seconds to stack 300 NCFs. The N^{th} -root
 376 method is the second fastest method following the Linear stack. In terms of the computational performance, these methods all
 377 scale nearly linearly with different data size.

378 5 CHOICE OF STACKING METHOD

379 In this section, we discuss the choice of stacking methods for different applications utilizing NCFs. We focus on the following
 380 major applications: 1) tomography of velocity structures, 2) monitoring of transient velocity changes, and 3) characterization of
 381 anelastic properties. These three research applications utilize different information from the NCFs: 1) seismic velocity tomog-
 382 raphy using surface waves requires dispersion information of the ballistic phases, 2) seismic monitoring requires dispersion
 383 and slight variations in phase information of the ballistic phases and/or the coda waves, and 3) the study of anelastic proper-
 384 ties for attenuation imaging and ground motion prediction relies on relative amplitudes of the ballistic phases. Although the
 385 performance could vary with different datasets, we provide here advantages and limitations for the stacking methods for each
 386 application, which we summarize in Table 1.

Applications	Evaluation metrics	Recommendations
Velocity tomography (5.1)	Signal-to-noise ratio (4.1), surface wave dispersion (4.2), and computational expenses (4.6)	Raw: Robust, [Linear, ACF] One-bit: Linear, Robust, Selective, ACF, Cluster
Monitoring (5.2)	Signal-to-noise ratio (4.1), surface-wave dispersion (4.2), convergence of short-term stacks to the long-term stack (4.3), transient phase changes (4.4), and computational expenses (4.6)	Raw: Robust, [Linear, tf-PWS] One-bit: Linear, Robust, Selective, [tf-PWS]
Anelastic properties (5.3)	Signal-to-noise ratio (4.1), surface wave dispersion (4.2), peak amplitudes of ballistic phases (4.5), and computational expenses (4.6)	Raw: Robust, [Linear, ACF] One-bit: Robust, Cluster

Table 1. Our recommendations of stacking methods for major applications using NCFs based on the evaluation metrics in Section 4. The numbers in () are the section numbers in the text. Methods in [] are recommendations with conditions as discussed in the text. See Section 5 for detailed discussions.

387 5.1 Stacking for tomography of velocity structures

388 Ambient noise tomography normally extracts the surface wave information from the stack of all NCFs for each station pair (e.g.,
389 Bensen et al. 2007). Most commonly, we use the fundamental mode surface waves, though there are some studies using higher
390 modes for imaging (e.g., G. Wu et al. 2020). Our recommendation for seismic velocity tomography is based on the following
391 metrics: signal-to-noise ratio (Section 4.1), surface wave dispersion (Section 4.2), and computational expenses (Section 4.6).

392 Based on our examples in Section 4.1, except for the OBS-OBS station pairs, the PWS method produces stacks with the
393 highest average SNRs, though with a large variance (Figs 4-10). The stacks using the N^{th} -root method also have relatively high
394 SNRs. Other stacking methods perform at a comparable level in terms of the SNRs of the ballistic phases. The phase dispersion
395 is better recovered using Robust and tf-PWS methods for Raw NCFs. The Linear and Selective methods also perform for
396 frequencies above 0.14 Hz, though the variability in the dispersion curves is notably high, particularly for the Selective method
397 (Figs 12a, 12c and 14a). The ACF method performs well at frequencies below 0.4 Hz. When using One-bit NCFs, all but the
398 PWS and N^{th} -root methods perform well overall in the dispersion analysis (Figs 13 and 14b). The relatively strong variability
399 in our example (Fig. 13d) using the Cluster method seems undesirable for tomographic study. The high computational cost
400 of tf-PWS method makes it impractical for processing large data sets for tomographic imaging (Fig. 19). In summary, our
401 recommendations for tomographic imaging are the Robust stacking for Raw NCFs and the Linear, Robust, Selective, Cluster,
402 and ACF methods for One-bit NCFs.

403 5.2 Stacking for monitoring of transient velocity changes

404 Seismic monitoring uses ballistic or coda wave interferometry to infer small changes in the subsurface from short-time stacks of
405 NCFs (e.g., F. Brenguier et al. 2008; Clements and Denolle 2018; Donaldson et al. 2019; Lobkis and Weaver 2003; Anne Ober-
406 mann and Hillers 2019). A shorter subset stacking time window enables a higher temporal resolution in seismic monitoring,
407 but the NCF stack may be unstable if the subset time window is too short (Hadziioannou et al. 2011). It is therefore important
408 to find the optimal length of the subset time window with converged stacks of the NCFs. Meanwhile, multi-frequency seismic

409 monitoring (e.g., Wang et al. 2019; C. Wu et al. 2016; Yuan et al. 2021) requires that the dispersion of surface waves remains
 410 stable through time. Therefore, our recommendation for seismic monitoring using ambient noise interferometry is based on the
 411 following additional metrics on top of those for tomography (Sections 4.1, 4.2, and 4.6): convergence of short-term stack to
 412 long-term stack (Section 4.3) and transient phase changes (Section 4.4).

413 Regarding the convergence metric, all stacking methods show comparable performance (Fig. 15). The relatively large
 414 variability in the rate of convergence using the Cluster stacking method may lead to artifacts in monitoring. The ACF method is
 415 also relatively slow in converging to the long-term stack. It is worth noting again that the rate/time of convergence also depends
 416 on the quality of specific datasets. The dispersion analyses are most stable using the Robust method for Raw NCFs. For One-bit
 417 NCFs, all but the PWS and N^{th} -root methods are appropriate choices (Figs 12-14).

418 For transient phase changes, all but the PWS method perform comparably well for all of the four examined examples (Fig.
 419 16). The tf-PWS method may be used to process the NCFs when long computational time are acceptable to the user, though
 420 computational efficiency could be improved to process large datasets (Fig. 19), or when using Graphic Processing Units (Zeng
 421 and Thurber 2016). In summary, our recommendations for seismic monitoring are the Robust method for Raw NCFs and the
 422 Linear, Robust, and Selective methods for One-bit NCFs. The Linear method can also be used for stacking Raw NCFs for a
 423 certain frequency range (>0.14 Hz in our examples).

424 5.3 Stacking for characterization of anelastic properties

425 The relative amplitudes of NCFs have been used to characterize the seismic attenuation properties of the Earth's lithosphere
 426 (Prieto et al. 2009) and the ground motion patterns (e.g., Denolle et al. 2013, 2014; Viens et al. 2017). Therefore, in addition
 427 to the metrics pertinent to tomography (Sections 4.1, 4.2, and 4.6), our recommendation for the characterization of anelastic
 428 properties using NCFs also evaluates the stability of peak absolute amplitudes of ballistic phases (Section 4.5).

429 Mitchell (1995) measured attenuation from a compilation global earthquake records from a variety of tectonic settings,
 430 including active margins, which are similar to the setting for the XZ linear array at the Cascadia margin. Because it is measured
 431 from earthquake surface-wave data, we argue that the attenuation parameter by Mitchell (1995) could serve as an independent
 432 benchmark in our evaluation. With this criterion, the Linear, Robust, Cluster, and ACF stacking methods are ranked as the top
 433 four among all of the methods for Raw NCFs (Fig. 17). However, the requirement of a reliable measurement of frequency-
 434 dependent attenuation and dispersion (Figs 12 and 14a) would narrow down the choice to Robust stacking. For One-bit NCFs,
 435 the Robust and Cluster stacking methods rank the best among all methods. Our recommendations for attenuation and ground
 436 motion studies, or any applications utilizing relative amplitudes, are the Robust method for Raw NCFs and the Robust and
 437 Cluster methods for One-bit NCFs. Similar to the research applications of velocity tomography and monitoring using ambient
 438 noise interferometry, the Linear and ACF methods could be used for certain frequency ranges (i.e., >0.14 Hz for Linear method
 439 and ≤ 0.4 Hz for ACF method in our examples).

440 **6 CONCLUSIONS**

441 NCFs are widely used in seismic velocity and attenuation imaging, monitoring, and ground motion analyses. The stacking
442 of NCFs over longer time periods is needed for most applications utilizing NCFs to increase the strength of the coherent
443 signals. There have been many temporal stacking methods developed to improve the stacking of NCFs. We compare eight
444 temporal stacking methods, including Linear, Robust, Selective, Cluster, Phase-Weighted, time-frequency Phase-Weighted,
445 N^{th} -root, and Adaptive Covariance Filter stacking methods, to investigate their performance to enhance the quality of the
446 stacked NCF. We examine the performance of these methods with six metrics, including signal-to-noise ratios, surface-wave
447 phase velocity dispersion, convergence of short-term stacks to the long-term stack, transient phase changes, peak amplitudes,
448 and computational expenses. Our analyses demonstrate that although all methods are able to retrieve clear ballistic phases, their
449 spectral contents and peak amplitudes vary significantly across methods. Based on multiple evaluation metrics, we recommend
450 the Robust method for seismic velocity tomography using Raw NCFs. All methods except for Phase-Weighted, time-frequency
451 phase-weighted, and N^{th} -root stacking methods are good choices for tomography using One-bit NCFs. For seismic monitoring,
452 which often involves stacking over subset time windows, the Robust method would be the best choice for Raw NCFs. For
453 monitoring using One-bit NCFs, the Linear, Robust, and Selective stacking methods are all preferred choices. For applications
454 utilizing relative amplitude information, the Robust stacking should be used for Raw NCFs while both the Robust and Cluster
455 stacking methods perform well for One-bit NCFs. The findings in this study provide a practical guideline in choosing the
456 appropriate stacking method for major applications utilizing NCFs. The open-source computer codes produced in this study
457 can also be used for general time series stacking analyses.

458 **ACKNOWLEDGMENTS**

459 This research has been funded by the startup funding of Purdue University for Xiaotao Yang, ARC grant DE220100907
460 to Chengxin Jiang, and NSF grant EAR1749556 to Marine Denolle. The seismic waveforms were downloaded from IRIS
461 Data Management Center and processed using *SeisGo* (<https://doi.org/10.5281/zenodo.5873724>), built upon *ObsPy*
462 (Beyreuther et al. 2010) and *NoisePy* (Jiang and Denolle 2020). All Python scripts and Jupyter notebooks used in processing and
463 visualizing the data and stacking results are available at https://github.com/xyangpsp/Paper_OptimalStacking and
464 are archived on Zenodo (<https://doi.org/10.5281/zenodo.6363585>). The computer codes for the stacking methods are
465 available as a standalone Python package, *StackMaster*, which is archived on Zenodo ([https://doi.org/10.5281/zenodo.](https://doi.org/10.5281/zenodo.5951013)
466 [5951013](https://doi.org/10.5281/zenodo.5951013)) and is accessible on Python Package Index (<https://pypi.org/project/stackmaster>). **Author Contributions:**
467 X. Yang and M. Denolle conveyed the idea for the project. X. Yang conducted the project, tested all computer codes, and lead
468 the writing of the manuscript. J. Bryan and K. Okubo worked on the selective stacking method. X. Yang developed the Cluster
469 stacking method. C. Jiang, M. Denolle, X. Yang, and T. Clements all contributed in implementation of the stacking methods.
470 All authors contributed in writing the manuscript.

471 Data from the TA network were made freely available as part of the EarthScope USArray facility, operated by Incorporated
472 Research Institutions for Seismology (IRIS) and supported by the National Science Foundation, under Cooperative Agreements
473 EAR-1261681.

474 **References**

- 475 Baig, A. M., M. Campillo, and F. Brenguier (2009). “Denoising seismic noise cross correlations”. In: *Journal of Geophysical Research: Solid Earth* 114.8, pp. 1–12. ISSN: 21699356. DOI: 10.1029/2008JB006085.
- 476
- 477 Bensen, G. D. et al. (2007). “Processing seismic ambient noise data to obtain reliable broad-band surface wave dispersion measurements”. In: *Geophysical Journal International* 169.3, pp. 1239–1260. ISSN: 0956-540X. DOI: 10.1111/j.1365-246X.2007.03374.x. eprint: <http://oup.prod.sis.lan/gji/article-pdf/169/3/1239/6082124/169-3-1239.pdf>. URL: <https://doi.org/10.1111/j.1365-246X.2007.03374.x>.
- 478
- 479
- 480
- 481 Beyreuther, Moritz et al. (2010). “ObsPy: A Python Toolbox for Seismology”. In: *Seismological Research Letters* 81.3, pp. 530–533. ISSN: 0895-0695. DOI: 10.1785/gssrl.81.3.530. eprint: <https://pubs.geoscienceworld.org/ssa/srl/article-pdf/81/3/530/2762059/530.pdf>. URL: <https://doi.org/10.1785/gssrl.81.3.530>.
- 482
- 483
- 484 Birtbill, J W et al. (1968). “Eliminating False Alarms when detecting Seismic Events Automatically”. In: *Nature* 1968 217:5128 217 (5128), pp. 533–534. ISSN: 1476-4687. DOI: 10.1038/217533A0. URL: <https://www-nature-com.ezproxy.lib.purdue.edu/articles/217533a0>.
- 485
- 486
- 487 Brenguier, F. et al. (2008). “Postseismic Relaxation Along the San Andreas Fault at Parkfield from Continuous Seismological Observations”. In: *Science* 321.5895, pp. 1478–1481. DOI: 10.1126/science.1160943.
- 488
- 489 Brenguier, Florent et al. (2008). “Towards forecasting volcanic eruptions using seismic noise”. In: *Nature Geoscience* 1.2, pp. 126–130. ISSN: 1752-0908. DOI: 10.1038/NGE0104. arXiv: 0706.1935. URL: <https://www-nature-com.ezproxy.lib.purdue.edu/articles/ngeo104>.
- 490
- 491
- 492 Clements, Timothy and Marine A Denolle (2018). “Tracking Groundwater Levels Using the Ambient Seismic Field”. In: *Geophysical Research Letters* 45.13, pp. 6459–6465. ISSN: 19448007. DOI: 10.1029/2018GL077706. URL: <https://doi.org/10.1029/2018GL077706>.
- 493
- 494
- 495 Denolle, Marine A et al. (2013). “Ground motion prediction of realistic earthquake sources using the ambient seismic field”. In: *JOURNAL OF GEOPHYSICAL RESEARCH: SOLID EARTH* 118, pp. 2102–2118. DOI: 10.1029/2012JB009603. URL: www.data.secc.org.
- 496
- 497 — (2014). “Strong Ground Motion Prediction Using Virtual Earthquakes”. In: *Science* 343.6169, pp. 399–403. DOI: 10.1126/science.1245678. eprint: <https://www.science.org/doi/pdf/10.1126/science.1245678>. URL: <https://www.science.org/doi/abs/10.1126/science.1245678>.
- 498
- 499
- 500 Denolle, Marine A et al. (2018). “Strong shaking predicted in Tokyo from an expected M7+ Itoigawa-Shizuoka earthquake”. In: *Journal of Geophysical Research: Solid Earth* 123.5, pp. 3968–3992.
- 501
- 502 Donaldson, C. et al. (2019). “Crustal seismic velocity responds to a magmatic intrusion and seasonal loading in Iceland’s Northern Volcanic Zone”. In: *Science Advances* 5.11. ISSN: 23752548. DOI: 10.1126/sciadv.aax6642.
- 503
- 504 Du, Zhijun, G. R. Foulger, and Weijian Mao (2000). “Noise reduction for broad-band, three-component seismograms using data-adaptive polarization filters”. In: *Geophysical Journal International* 141.3, pp. 820–828. ISSN: 0956-540X. DOI: 10.1046/j.1365-246x.2000.00156.x. eprint: <https://academic.oup.com/gji/article-pdf/141/3/820/1687588/141-3-820.pdf>. URL: <https://doi.org/10.1046/j.1365-246x.2000.00156.x>.
- 505
- 506
- 507
- 508 Ermert, Laura, Antonio Villasenor, and Andreas Fichtner (2016). “Cross-correlation imaging of ambient noise sources”. In: *Geophysical Journal International* 204.1, pp. 347–364.
- 509

- 510 Ermert, Laura A et al. (2021). “Multifrequency inversion of global ambient seismic sources”. In: *Geophysical Journal International* 225.3,
511 pp. 1616–1623.
- 512 Feng, Kuan-Fu et al. (2021). “Controls on Seasonal Variations of Crustal Seismic Velocity in Taiwan Using Single-Station Cross-Component
513 Analysis of Ambient Noise Interferometry”. In: *Journal of Geophysical Research: Solid Earth* 126.11, e2021JB022650.
- 514 Feng, Lili and Michael H. Ritzwoller (2019). “A 3-D Shear Velocity Model of the Crust and Uppermost Mantle Beneath Alaska Including
515 Apparent Radial Anisotropy”. In: *Journal of Geophysical Research: Solid Earth* 124.10, pp. 10468–10497. ISSN: 21699356. DOI:
516 10.1029/2019JB018122.
- 517 Hadziioannou, Céline et al. (2011). “Improving temporal resolution in ambient noise monitoring of seismic wave speed”. In: *Journal of*
518 *Geophysical Research: Solid Earth* 116.B7.
- 519 Jiang, Chengxin and Marine A Denolle (2020). “NoisePy: A New High-Performance Python Tool for Ambient-Noise Seismology”. In:
520 *Seismological Research Letters*. ISSN: 0895-0695. DOI: 10.1785/0220190364. eprint: [https://pubs.geoscienceworld.org/
521 srl/article-pdf/doi/10.1785/0220190364/4974556/srl-2019364.1.pdf](https://pubs.geoscienceworld.org/srl/article-pdf/doi/10.1785/0220190364/4974556/srl-2019364.1.pdf). URL: [https://doi.org/10.1785/
522 0220190364](https://doi.org/10.1785/0220190364).
- 523 Kanasewich, E. R., C. D. Hemmings, and T. Alpaslan (1973). “ N^{th} -Root Stack Nonlinear Multichannel Filter”. In:
524 <http://dx.doi.org/10.1190/1.1440343> 38 (2), pp. 327–338. ISSN: 0016-8033. DOI: 10.1190/1.1440343. URL: [https://library.
525 seg.org/doi/abs/10.1190/1.1440343](https://library.seg.org/doi/abs/10.1190/1.1440343).
- 526 Kwak, Sangmin et al. (2017). “Investigating the capability to extract impulse response functions from ambient seismic noise using a mine
527 collapse event”. In: *Geophysical Research Letters* 44.19, pp. 9653–9662.
- 528 Li, Guoliang et al. (2017). “An investigation of time–frequency domain phase-weighted stacking and its application to phase-velocity
529 extraction from ambient noise’s empirical Green’s functions”. In: *Geophysical Journal International* 212.2, pp. 1143–1156. ISSN:
530 0956-540X. DOI: 10.1093/gji/ggx448. eprint: [https://academic.oup.com/gji/article-pdf/212/2/1143/22297175/
531 ggx448.pdf](https://academic.oup.com/gji/article-pdf/212/2/1143/22297175/ggx448.pdf). URL: <https://doi.org/10.1093/gji/ggx448>.
- 532 Liu, Guochang et al. (2009). “Stacking seismic data using local correlation”. In: *Geophysics* 74.3, pp. V43–V48. DOI: 10.1190/1.
533 3085643.
- 534 Lobkis, Oleg I. and Richard L. Weaver (2003). “Coda-Wave Interferometry in Finite Solids: Recovery of P -to- S Conversion Rates in an
535 Elastodynamic Billiard”. In: *Phys. Rev. Lett.* 90 (25), p. 254302. DOI: 10.1103/PhysRevLett.90.254302. URL: [https://link.
536 aps.org/doi/10.1103/PhysRevLett.90.254302](https://link.aps.org/doi/10.1103/PhysRevLett.90.254302).
- 537 Millet, F., T. Bodin, and S. Rondenay (2019). “Multimode 3-D Kirchhoff Migration of Receiver Functions at Continental Scale”. In:
538 *Journal of Geophysical Research: Solid Earth* 124.8, pp. 8953–8980. DOI: 10.1029/2018JB017288. eprint: [https://agupubs.
539 onlinelibrary.wiley.com/doi/pdf/10.1029/2018JB017288](https://agupubs.onlinelibrary.wiley.com/doi/pdf/10.1029/2018JB017288). URL: [https://agupubs.onlinelibrary.wiley.com/doi/
540 abs/10.1029/2018JB017288](https://agupubs.onlinelibrary.wiley.com/doi/abs/10.1029/2018JB017288).
- 541 Mitchell, Brian J (1995). “Anelastic structure and evolution of the continental crust and upper mantle from seismic surface wave attenuation”.
542 In: *Reviews of Geophysics* 33.4, pp. 441–462.
- 543 Moreau, L et al. (2017). “Improving ambient noise correlation functions with an SVD-based Wiener filter”. In: *Geophys. J. Int.* 211.1,
544 pp. 418–426. DOI: 10.1093/gji/ggx306.

- 545 Nabelek, J. et al. (1993). "A high-resolution image of the Cascadia subduction zone from teleseismic converted phases recorded by a
546 broadband seismic array". In: *Eos Transaction* 74.43, p. 431.
- 547 Nakata, Nori et al. (2015). "Body wave extraction and tomography at Long Beach, California, with ambient-noise interferometry". In: *J.*
548 *Geophys. Res.* 120.2, pp. 1159–1173. DOI: 10.1002/2015JB011870.
- 549 Obermann, A. et al. (2014). "Seismic noise correlations to image structural and mechanical changes associated with the Mw 7.9 2008
550 Wenchuan earthquake". In: *Journal of Geophysical Research: Solid Earth* 119.4, pp. 3155–3168. ISSN: 21699356. DOI: 10.1002/
551 2013JB010932.
- 552 Obermann, Anne and Gregor Hillers (2019). "Chapter Two - Seismic time-lapse interferometry across scales". In: *Recent Advances in*
553 *Seismology*. Ed. by Cedric Schmelzbach. Vol. 60. Advances in Geophysics. Elsevier, pp. 65–143. DOI: [https://doi.org/10.1016/](https://doi.org/10.1016/bs.agph.2019.06.001)
554 [bs.agph.2019.06.001](https://www.sciencedirect.com/science/article/pii/S0065268719300020). URL: <https://www.sciencedirect.com/science/article/pii/S0065268719300020>.
- 555 Olivier, G. et al. (2015). "Body-wave reconstruction from ambient seismic noise correlations in an underground mine". In: *GEOPHYSICS*
556 80.3, KS11–KS25. DOI: 10.1190/geo2014-0299.1. eprint: <https://doi.org/10.1190/geo2014-0299.1>. URL: <https://doi.org/10.1190/geo2014-0299.1>.
- 557 //doi.org/10.1190/geo2014-0299.1.
- 558 Olivier, G. et al. (2019). "Decrease in Seismic Velocity Observed Prior to the 2018 Eruption of Kīlauea Volcano With Ambient Seismic
559 Noise Interferometry". In: *Geophysical Research Letters* 46.7, pp. 3734–3744. ISSN: 19448007. DOI: 10.1029/2018GL081609.
- 560 Pavlis, Gary L. and Frank L. Vernon (2010). "Array processing of teleseismic body waves with the USArray". In: *Computers & Geo-*
561 *sciences* 36.7, pp. 910–920. ISSN: 0098-3004. DOI: <https://doi.org/10.1016/j.cageo.2009.10.008>. URL: [http://](http://www.sciencedirect.com/science/article/pii/S0098300410001159)
562 www.sciencedirect.com/science/article/pii/S0098300410001159.
- 563 Prieto, G. A., J. F. Lawrence, and G. C. Beroza (2009). "Anelastic Earth structure from the coherency of the ambient seismic field". In:
564 *Journal of Geophysical Research: Solid Earth* 114.7, pp. 1–15. ISSN: 21699356. DOI: 10.1029/2008JB006067.
- 565 Rost, Sebastian and Christine Thomas (2002). "Array seismology: Methods and applications". In: *Reviews of geophysics* 40.3, pp. 2–1.
- 566 Rückemann, Claus-Peter CP (2012). "Comparison of Stacking Methods Regarding Processing and Computing of Geoscientific Depth
567 Data". In: *In Proc. Fourth International Conference on Advanced Geographic Information Systems, Applications, and Services (GEO-*
568 *Processing 2012)* c, pp. 35–40. URL: [http://www.thinkmind.org/index.php?view=article%7B%5C%7D](http://www.thinkmind.org/index.php?view=article%7B%5C%7Darticleid=geoprocessing%7B%5C%7D2012%7B%5C%7D2%7B%5C%7D10%7B%5C%7D30050)
569 [articleid=geoprocessing%7B%5C%7D2012%7B%5C%7D2%7B%5C%7D10%7B%5C%7D30050](http://www.thinkmind.org/index.php?view=article%7B%5C%7Darticleid=geoprocessing%7B%5C%7D2012%7B%5C%7D2%7B%5C%7D10%7B%5C%7D30050).
- 570 Samson, J. C. and J. V. Olson (1981). "Data-adaptive polarization filters for multichannel geophysical data". In: *GEOPHYSICS* 46.10,
571 pp. 1423–1431. DOI: 10.1190/1.1441149. eprint: <https://doi.org/10.1190/1.1441149>. URL: [https://doi.org/10.1190/](https://doi.org/10.1190/1.1441149)
572 [1.1441149](https://doi.org/10.1190/1.1441149).
- 573 Schimmel, M. and J. Gallart (2007). "Frequency-dependent phase coherence for noise suppression in seismic array data". In: *Journal of*
574 *Geophysical Research: Solid Earth* 112.4, pp. 1–14. ISSN: 21699356. DOI: 10.1029/2006JB004680.
- 575 Schimmel, M. and H. Paulssen (1997). "Noise reduction and detection of weak, coherent signals through phase-weighted stacks". In:
576 *Geophysical Journal International* 130.2, pp. 497–505. ISSN: 0956540X. DOI: 10.1111/j.1365-246X.1997.tb05664.x.
- 577 Schimmel, M., E. Stutzmann, and J. Gallart (2011). "Using instantaneous phase coherence for signal extraction from ambient noise data
578 at a local to a global scale". In: *Geophysical Journal International* 184.1, pp. 494–506. ISSN: 0956540X. DOI: 10.1111/j.1365-
579 [246X.2010.04861.x](https://doi.org/10.1111/j.1365-246X.2010.04861.x).

- 580 Seats, Kevin J, Jesse F Lawrence, and German A Prieto (2012). “Improved ambient noise correlation functions using Welch’s method”. In:
581 *Geophysical Journal International* 188.2, pp. 513–523.
- 582 Shapiro, Nikolai M. et al. (2005). “High-resolution surface-wave tomography from ambient seismic noise”. In: *Science* 307 (5715),
583 pp. 1615–1618. ISSN: 00368075. DOI: 10.1126/SCIENCE.1108339. URL: www.iris.iris.edu/USArray.
- 584 Shen, Yang et al. (2012). “An Improved Method to Extract Very-Broadband Empirical Green’s Functions from Ambient Seismic Noise”.
585 In: *Bulletin of the Seismological Society of America* 102.4, pp. 1872–1877. ISSN: 0037-1106. DOI: 10.1785/0120120023. eprint:
586 <https://pubs.geoscienceworld.org/bssa/article-pdf/102/4/1872/2667786/1872.pdf>. URL: <https://doi.org/10.1785/0120120023>.
587 1785/0120120023.
- 588 Stehly, L, Michel Campillo, and NM Shapiro (2006). “A study of the seismic noise from its long-range correlation properties”. In: *Journal*
589 *of Geophysical Research: Solid Earth* 111.B10.
- 590 Stehly, Laurent and Pierre Boué (2017). “On the interpretation of the amplitude decay of noise correlations computed along a line of
591 receivers”. In: *Geophysical Journal International* 209.1, pp. 358–372. ISSN: 0956-540X. DOI: 10.1093/gji/ggx021. eprint: <https://academic.oup.com/gji/article-pdf/209/1/358/10763137/ggx021.pdf>. URL: <https://doi.org/10.1093/gji/ggx021>.
592 //academic.oup.com/gji/article-pdf/209/1/358/10763137/ggx021.pdf. URL: <https://doi.org/10.1093/gji/ggx021>.
593 ggx021.
- 594 Stockwell, R. G. (2007). “A basis for efficient representation of the S-transform”. In: *Digital Signal Processing: A Review Journal* 17.1,
595 pp. 371–393. ISSN: 10512004. DOI: 10.1016/j.dsp.2006.04.006.
- 596 Stockwell, R. G., L. Mansinha, and R. P. Lowe (1996). “Localization of the complex spectrum: The S transform”. In: *IEEE Transactions*
597 *on Signal Processing* 44.4, pp. 998–1001. ISSN: 1053587X. DOI: 10.1109/78.492555.
- 598 Tavenard, Romain et al. (2020). “Tslern, A Machine Learning Toolkit for Time Series Data”. In: *Journal of Machine Learning Research*
599 21.118, pp. 1–6. URL: <http://jmlr.org/papers/v21/20-091.html>.
- 600 Thangraj, J. S. and J. Pulliam (2021). “Towards real-time assessment of convergence criteria in seismic interferometry: Selective stacking
601 of cross-correlations at the San Emidio geothermal field”. In: *Journal of Applied Geophysics* 193, p. 104426. ISSN: 0926-9851. DOI:
602 <https://doi.org/10.1016/j.jappgeo.2021.104426>. URL: <https://www.sciencedirect.com/science/article/pii/S0926985121001737>.
603 S0926985121001737.
- 604 Thurber, Clifford H. et al. (2014). “Phase-weighted stacking applied to low-frequency Earthquakes”. In: *Bulletin of the Seismological*
605 *Society of America* 104.5, pp. 2567–2572. ISSN: 19433573. DOI: 10.1785/0120140077.
- 606 Tian, Ye and Michael H. Ritzwoller (2017). “Improving ambient noise cross-correlations in the noisy ocean bottom environment of the Juan
607 de Fuca plate”. In: *Geophysical Journal International* 210.3, pp. 1787–1805. ISSN: 0956-540X. DOI: 10.1093/gji/ggx281. eprint:
608 <https://academic.oup.com/gji/article-pdf/210/3/1787/19194924/ggx281.pdf>. URL: <https://doi.org/10.1093/gji/ggx281>.
609 gji/ggx281.
- 610 Viens, Loïc and Marine A Denolle (2019). “Long-period ground motions from past and virtual megathrust earthquakes along the Nankai
611 Trough, Japan”. In: *Bulletin of the Seismological Society of America* 109.4, pp. 1312–1330.
- 612 Viens, Loïc and Tomotaka Iwata (2020). “Improving the Retrieval of Offshore-Onshore Correlation Functions With Machine Learning”. In:
613 *Journal of Geophysical Research: Solid Earth* 125.8, pp. 1–19. ISSN: 21699356. DOI: 10.1029/2020JB019730.
- 614 Viens, Loïc et al. (2017). “Retrieving impulse response function amplitudes from the ambient seismic field”. In: *Geophysical Journal*
615 *International* 210.1, pp. 210–222. ISSN: 1365246X. DOI: 10.1093/gji/ggx155.

- 616 Wang, Qing-Yu et al. (2017). “Seasonal crustal seismic velocity changes throughout Japan”. In: *Journal of Geophysical Research: Solid*
617 *Earth* 122.10, pp. 7987–8002.
- 618 Wang, Qing-Yu et al. (2019). “Evidence of changes of seismic properties in the entire crust beneath Japan after the M w 9.0, 2011 Tohoku-
619 oki earthquake”. In: *Journal of Geophysical Research: Solid Earth* 124.8, pp. 8924–8941.
- 620 Webb, Spahr C. (1998). “Broadband seismology and noise under the ocean”. In: *Reviews of Geophysics* 36.1, pp. 105–142. ISSN: 87551209.
621 DOI: 10.1029/97RG02287.
- 622 Wu, Chunquan et al. (2016). “Constraining depth range of S wave velocity decrease after large earthquakes near Parkfield, California”. In:
623 *Geophysical Research Letters* 43.12, pp. 6129–6136.
- 624 Wu, Gaoxiong et al. (2020). “Shear Velocity Inversion Using Multimodal Dispersion Curves From Ambient Seismic Noise Data of US-
625 Array Transportable Array”. In: *Journal of Geophysical Research: Solid Earth* 125.1, pp. 1–14. ISSN: 2169-9313. DOI: 10.1029/
626 2019jb018213.
- 627 Wu, Sin-Mei et al. (2021). “Imaging the Subsurface Plumbing Complex of Steamboat Geyser and Cistern Spring With Hydrothermal
628 Tremor Migration Using Seismic Interferometry”. In: *Journal of Geophysical Research: Solid Earth* 126 (4). ISSN: 21699356. DOI:
629 10.1029/2020JB021128.
- 630 Yang, Xiaotao and Haiying Gao (2018). “Full-Wave Seismic Tomography in the Northeastern United States: New Insights Into the Uplift
631 Mechanism of the Adirondack Mountains”. In: *Geophysical Research Letters* 45.12. ISSN: 19448007. DOI: 10.1029/2018GL078438.
- 632 — (2020). “Segmentation of the Aleutian-Alaska Subduction Zone Revealed by Full-Wave Ambient Noise Tomography: Implications for
633 the Along-Strike Variation of Volcanism”. In: *Journal of Geophysical Research: Solid Earth* 125.11, pp. 1–20. ISSN: 21699356. DOI:
634 10.1029/2020JB019677.
- 635 Yang, Xiaotao et al. (2019). “A Comprehensive Quality Analysis of Empirical Green’s Functions at Ocean-Bottom Seismometers in Cas-
636 cadia”. In: *Seismological Research Letters* 90.2A, pp. 744–753. ISSN: 0895-0695. DOI: 10.1785/0220180273. eprint: <https://pubs.geoscienceworld.org/srl/article-pdf/90/2A/744/4655388/srl-2018273.1.pdf>. URL: <https://doi.org/10.1785/0220180273>.
- 637
638
- 639 Yang, Xiaotao et al. (2022a). *SeisGo: A ready-to-go Python toolbox for seismic data analysis*. Computer Software. Version v0.7.0. DOI:
640 10.5281/zenodo.5873724. URL: <https://doi.org/10.5281/zenodo.5873724>.
- 641 Yang, Xiaotao et al. (2022b). *StackMaster: A Collection of Methods for Data Stacking*. Computer Software. Version v1.0.3. This replaces
642 StackPy/StackMaster v1.0.3. DOI: 10.5281/zenodo.5951013. URL: <https://doi.org/10.5281/zenodo.5951013>.
- 643 Yang, Yingjie and Michael H. Ritzwoller (2008). “Characteristics of ambient seismic noise as a source for surface wave tomography”. In:
644 *Geochemistry, Geophysics, Geosystems* 9.2. ISSN: 15252027. DOI: 10.1029/2007GC001814.
- 645 Yang, Zhuo, Congcong Yuan, and Marine A Denolle (2022). “Detecting Elevated Pore Pressure due to Wastewater Injection Using Ambient
646 Noise Monitoring”. In: *The Seismic Record* 2.1, pp. 38–49.
- 647 Yao, Huajian, Robert D. van der Hilst, and Maarten V. de Hoop (2006). “Surface-wave array tomography in SE Tibet from ambient seismic
648 noise and two-station analysis - I. Phase velocity maps”. In: *Geophysical Journal International* 166.2, pp. 732–744. ISSN: 0956540X.
649 DOI: 10.1111/j.1365-246X.2006.03028.x.
- 650 Yuan, Congcong, Jared Bryan, and Marine A Denolle (2021). “Numerical comparison of time-, frequency-, and wavelet-domain methods
651 for coda wave interferometry”. In: *Geophysical Journal International*, pp. 828–846. ISSN: 0956-540X. DOI: 10.1093/gji/ggab140.

652 Zeng, Xiangfang and Clifford H. Thurber (2016). “A graphics processing unit implementation for time–frequency Phase-Weighted Stack-
653 ing”. In: *Seismological Research Letters* 87.2A, pp. 358–362. ISSN: 0895-0695. DOI: 10.1785/0220150192. eprint: [https://pubs.
654 geoscienceworld.org/srl/article-pdf/87/2A/358/2771201/358.pdf](https://pubs.geoscienceworld.org/srl/article-pdf/87/2A/358/2771201/358.pdf). URL: <https://doi.org/10.1785/0220150192>.